# Influence of Grain Boundary Energy Anisotropy on the Evolution of Grain Boundary Network Structure during 3D Anisotropic Grain Growth

José D. Niño[a,*], Oliver K. Johnson[a]

[a]*Department of Mechanical Engineering, Brigham Young University, Provo, UT 84602, USA*

**Abstract**

In this paper, we present the results of grain growth simulations in three-dimensions using an existing level set method. Most of the previous grain growth studies have been either isotropic or, if they are not isotropic, consider simplified models of anisotropy. We perform these simulations using three different grain boundary (GB) energy functions (a realistic 5D GB energy function, a Read-Shockley energy model that depends only on disorientation angle, and an isotropic GB energy model). We compare the results in terms of several statistical microstructural descriptors (crystallographic texture, GB character distribution, triple junction distribution (TJD), etc.). In addition to considering different energy models, we also compare the evolution of microstructures that have different initial crystallographic textures (fiber texture and random texture). We find that the morphological evolution of individual grains can be completely different depending on the GB energy function employed. However, we also find that certain spatially independent microstructural statistics (e.g. orientation distribution function, misorientation distribution function, and TJD) are similar at steady state for all of the tested GB energy functions.

*Keywords:* Grain growth, Grain Boundary Network, Anisotropy, GB Energy

## 1. Introduction

When a polycrystalline material is annealed, the microstructure coarsens (some grains grow while other shrink), resulting in an increase in the average grain size with time. This phenomenon is known as grain growth. During grain growth, the microstructure evolves to reduce the energy of the system by reducing the grain boundary (GB) area. GBs move toward their centers of curvature. In the absence of pinning [1] or drag phenomena [2] and if stored energy driving forces are neglected, the local velocity of a GB is proportional to the local curvature of the GB, and it is determined by the equation:

$$v = M\gamma\kappa \tag{1}$$

where $\kappa$ is the mean curvature of the GB, $M$ is the GB mobility, and $\gamma$ is the GB energy (also referred to as surface tension).

Due to the opacity of metals, experimental characterization of grain growth in three-dimensions is challenging. Recently developed non-destructive 4D characterization techniques like HEDM [3] and labDCT [4] are shedding new light on the subject [5–7]; however, these are not yet ubiquitous, and the vast majority of experimental microstructure characterization remains destructive and two-dimensional. Therefore, studies of three-dimensional grain growth have mainly relied on computational simulations.

A GB is characterized by five macroscopic crystallographic parameters. Three of the parameters define the misorientation between the adjacent grains, and the other two define the GB plane. The grain growth studies that consider anisotropic GB energy usually employ simplified models for which

*Corresponding author.
*Email address:* josens2101@byu.edu (José D. Niño)

GB energy depends only on lattice misorientation. Nevertheless, it has been observed [8] that the GB plane also impacts the evolution of the GB network during grain growth. Consequently, to have a better understanding of anisotropic grain growth, it is necessary to model microstructural transformations under realistic conditions—that is, considering the misorientation as well as the GB normal.

Algorithms for computational simulations of grain growth include a variety of probabilistic and deterministic methods. Probabilistic methods include Monte Carlo Potts models [9–13] and cellular automata [14]. Deterministic methods include Phase field [15–22], Level set [23–32], and Front tracking methods [33–36].

Classical theories of grain growth assume isotropic conditions [37–39], and many simulations have been performed under these assumptions [23, 24, 33–36, 40]. It has been shown that the GB energy has a more significant effect on grain growth than GB mobility [11, 12]; thus, several simulations consider isotropic mobility but with anisotropic GB energy. Most computational anisotropic grain growth studies [9–13, 25–30, 32] use the Read-Shockley relationship [41], which considers the misorientation, but neglects the plane normal. One of the main advantages of the Read-Shockley function is that it is very computationally inexpensive to use. Esedoḡlu et al. [27] proposed a level set method that simulates the mean curvature motion of networks of interfaces under arbitrary GB energies. They used this algorithm to perform anisotropic 3D grain growth simulations using the Read-Shockley model of GB energy [25].

Only a few studies have performed simulations using energy models that consider the dependence of GB energy on all five crystallographic degrees of freedom. For instance, Kim et al. [17] performed three-dimensional simulations using a phase-field model. They obtained the GB energies from a GB energy database in BCC Fe [42]. The database contained 91 data points for each misorientation for a total of 69,251 GBs. To use the database during their grain growth simulation, they first calculated the normal vector of the point on a given GB for which they wanted to calculate the energy. Then, given the misorientation of that GB, they found the three nearest data points to that GB normal in the database. Finally, the desired GB energy was computed as the weighted average of these three data points. It is important to note that all the GB normals and misorientations were discretized.

In another study, Salama et al. [22] performed three-dimensional grain growth phase-field simulations. They studied the influence of the plane normal in grain growth using a hypothetical GB energy function proposed by Caginalp [43] and concluded that the inclination dependence of the GB energy has an impact on the microstructure evolution.

Recently, work has been done to develop fully anisotropic structure-property models for GBs [44, 45]. Bulatov, Reed, and Kumar [44] developed a continuous 5D interpolation function for GB energy in FCC metals that considers both the GB misorientation and the GB plane. This function, which we refer to as the BRK function, is built on the 5D crystallography of FCC GBs and molecular statics GB energy calculations [46]. The development of the BRK function has provided an opportunity to perform anisotropic simulations that consider all five degrees of freedom of a GB.

A recent grain growth study [47] suggested using the BRK function to explore the effects of the GB energy dependence on microstructure evolution. The BRK model has been incorporated by Hallberg in a level set formulation they recently developed [31]. They showed how a fully anisotropic (5D) GB energy function can be incorporated in a grain growth simulation study. In addition, by considering individual grains and individual triple-junctions, they demonstrated that GB energy anisotropy has a significant effect on the local microstructure, and that isotropic energy models will not accurately reproduce local morphological features.

In the present work, rather than focus on the effect of anisotropic GB energy on *local* microstructure morphology, we investigate how GB energy anisotropy affects global statistical descriptors and their evolutionary pathways, which requires larger polycrystalline simulations. Such fully anisotropic simulations that consider all five degrees of freedom in large polycrystalline microstructures for FCC metals have not yet been reported, and in spite of

almost seven decades of grain growth studies, there is still much about this important phenomenon that remains unknown. In particular: In what ways is the evolution of a microstructure different (or the same) when a realistic fully 5D GB energy function is employed vs. traditional simplified models? And how does the initial microstructure influence the evolution and the final state of the microstructure?

We performed fully anisotropic grain growth simulations in three dimensions (3D) using an existing level set method developed by Esedoḡlu [27]. Full anisotropy was achieved by implementing the BRK GB energy function. For comparison, we also performed isotropic and partially anisotropic (using the Read-Shockley function) grain growth simulations using the same initial microstructure. For each of the 3 GB energy functions (BRK, Read-Shockley, isotropic) we performed two sets of simulations to investigate the influence of the initial crystallographic texture. The first set used an initial microstructure with a random texture (typical of rotation recrystallization, extrusion, and uniaxial compression, [48–50]) and the second set used an initial microstructure with a perfect [001] fiber texture (typical of common manufacturing processes such as drawing, plain-strain rolling, and additive manufacturing [51–54]).

In Sections 2.1–2.3, we describe the level set method and the implementation of the energy functions. In Section 2.4, we provide validation examples. In Section 3, we present the statistical analysis of the large-scale simulation results. Finally, in Section 4, we discuss the influence of the initial texture on the resulting microstructure and the impact of GB energy on the evolution of the GB network.

## 2. Methods

### *2.1. Level set model*

In the present study, we built on a program developed by Esedoḡlu based on one of the algorithms described in [27]. The algorithm models the grains as distinct "phases," $\Sigma_i$, of a domain in 3 dimensions with periodic conditions. These phases interact through their boundaries, and the energy of the boundary equals the area of the boundary times the GB energy between the two grains that form the boundary. This algorithm simulates the mean curvature motion of networks of interfaces under arbitrary GB energies (i.e. GB energy models) in two steps, performed iteratively, as shown in Algorithm 1.

**Algorithm 1:** Original Algorithm [27]

At time step $t = (\delta t)(k+1)$:

1 Convolution step

$$\phi_i^k = G_{\delta t} * \sum_{j=1}^{N} \gamma_{i,j} \mathbb{1}_{\Sigma_j^k} \tag{2}$$

2 Thresholding step

$$\Sigma_i^{k+1} = \left\{ x : \phi_i^k(x) < \min_{j \neq i} \phi_i^k(x) \right\} \tag{3}$$

The first step is a GB energy weighted convolution between characteristic functions, $\mathbb{1}_{\Sigma_j^k}$, and the Gaussian kernel, $G_{\delta t}$. The convolution is performed in the Fourier domain over a discretized version of the microstructure (a grid of points that is equivalent to a voxelized representation of the microstructure). The second step is thresholding (or redistribution), which updates the state of the microstructure (i.e. the $\Sigma_i^{k+1}$, which define the grains).

In this algorithm, the GB energy determines the equilibrium dihedral angle condition at the triple junctions (TJs). Earlier work [11, 12] suggested that many of the statistics appear not to depend so much on the mobilities, but depend strongly on the GB energies and the equilibrium dihedral angle conditions at the junctions. The original algorithm enables the use of arbitrary GB energy models that depend only on misorientation; therefore, some adaptation was necessary to facilitate the use of models that include the dependence of the GB plane, as described in Section 2.2.2.

The algorithm we use leaves the convolution and thresholding steps of Algorithm 1 essentially unchanged, but adds two additional steps before them as shown in Algorithm 2.

Before the convolution step, the GB normal at each voxel that belongs to a GB is calculated. Thus the normal of a GB is not constant, but varies

**Algorithm 2:** Revised Algorithm

At time step $t = (\delta t)(k+1)$:

1 Calculate normals for every GB voxel

$$\mathbf{n}^S(\mathbf{r}) = [M_{100}(\mathbf{r}), M_{010}(\mathbf{r}), M_{001}(\mathbf{r})]^\intercal \quad (4)$$

$$\mathbf{n}^i(\mathbf{r}) = g_i^{-1}\mathbf{n}^S(\mathbf{r}) \quad (5)$$

2 Calculate fully anisotropic GB energy for every GB voxel

$$\gamma_{i,j}(\mathbf{r}) = \gamma\big(g_{ij}, \mathbf{n}^i(\mathbf{r})\big) \quad (6)$$

3 Convolution step

$$\phi_i^k = G_{\delta t} * \sum_{j=1}^{N} \gamma_{i,j}(\mathbf{r})\, \mathbb{1}_{\Sigma_j^k} \quad (7)$$

4 Thresholding step

$$\Sigma_i^{k+1} = \left\{ x : \phi_i^k(x) < \min_{j \neq i} \phi_i^k(x) \right\} \quad (8)$$

over its surface (and consequently so does the GB energy). Using the calculated normals and corresponding misorientations, we then obtain the GB energies of each GB voxel using the GB energy function. The convolution and thresholding steps are then performed as defined in the original algorithm. A detailed explanation of each of the two new steps is provided in Section 2.3 and Section 2.2, respectively.

### *2.1.1. Simulation parameters*

Using the level set method developed by Esedoḡlu and the BRK function, we performed several grain growth simulations using the same initial microstructure to investigate the effects of the GB energy and the texture on the evolution of the GB network. Simulations were performed in 3D on a cuboidal grid of $136 \times 136 \times 136$ voxels with periodic boundary conditions. The simulations were initialized in two steps (Fig. 1): first a three-dimensional polycrystalline microstructural template was constructed, then grain orientations were assigned before performing the actual anisotropic grain growth simulations. We describe these two initialization steps below.

Starting with a three-dimensional Voronoi tessellation containing 10,000 grains (Fig. 1a), we performed an initial stage of isotropic grain growth. Then, when 7,500 grains remained, we stopped the simulation and saved the resulting microstructure as the polycrystalline microstructure template (the starting point for the subsequent anisotropic simulations, as shown in Fig. 1b). By doing this, we avoided the initial transition period from a Voronoi microstructure to a grain growth microstructure [12].

After obtaining the microstructure template, each of the 7,500 grains were assigned a crystallographic orientation from either a uniform orientation distribution function (ODF) (Fig. 1c-e) or a [001] fiber textured ODF (Fig. 1f-h).

Samples from a uniform ODF were obtained by generating quaternions that were uniformly distributed over the half of $\mathbb{S}^3$ with positive first coordinate, where the quaternion coordinates are defined by

$$\mathbf{q} = \left[\cos\left(\frac{\omega}{2}\right),\ \sin\left(\frac{\omega}{2}\right)\mathbf{u}\right] \quad (9)$$

with $\omega$ representing the rotation angle and where $\mathbf{u}$ is a vector representing the axis of rotation.

Samples from the fiber textured ODF were obtained by generating rotation angles, $\omega$, that were uniformly distributed over $\mathbb{S}^1$. We then constructed quaternions having those rotation angles and a rotation axis of [001] (see Fig. 1f-h).

In both cases, the orientations were assigned uniformly at random to each grain. As we assign orientations to each grain of the microstructure, crystallographic constraints are satisfied by construction[1].

The subsequent anisotropic simulations were run until only $\sim$5 % (about 400) of the initial grains remained.

[1] Crystallographic consistency requires that the product of misorientations coordinating a triple junction result in the identity [56, 57], i.e. $g_{12}g_{23}g_{31} = I$. Because we assign grain orientations (rather than GB misorientations, which are instead computed from the assigned orientations), this relation is automatically respected by construction.

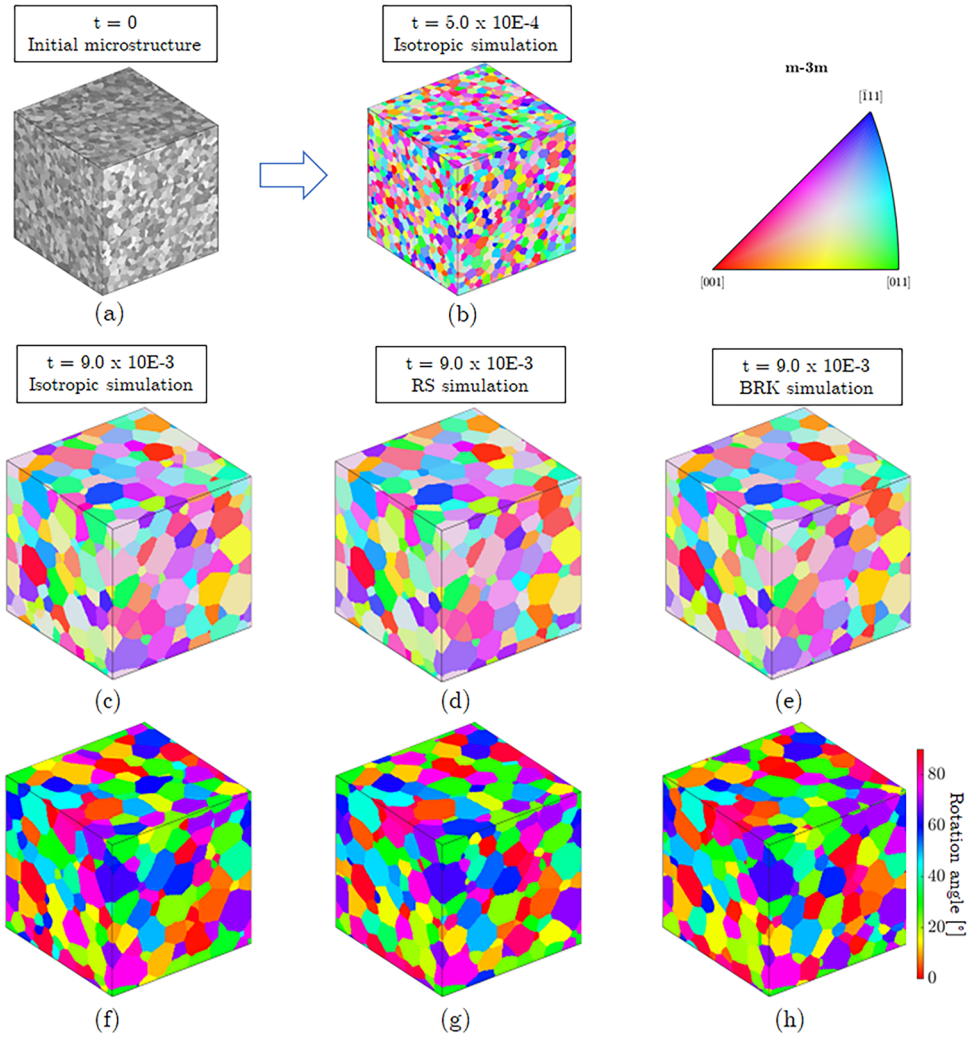


Figure 1: (a) Initial microstructure (10,000 grains). (b) Microstructure after initial isotropic simulation to obtain grain growth microstructure (7500 grains). Final microstructure from grain growth simulations assigning initial random texture under (c) isotropic GB energy, (d) anisotropic GB energy (using Read-Shockley), and (e) fully anisotropic GB energy (using BRK function). Final microstructure from grain growth simulations assigning initial fiber texture under (f) isotropic GB energy, (g) anisotropic GB energy (using Read-Shockley), and (f) fully anisotropic GB energy (using BRK function). Grain colors and corresponding color legend for (b)-(e) were constructed using MTEX [55].

### *2.2. Energy models*

During the simulations, at each time-step, each voxel that formed part of a GB was assigned a surface tension (GB energy) based on the chosen constitutive model. To understand how the use of a realistic and fully 5D anisotropic model for GB energy compares to previous work, we employed three different models for GB energy: isotropic, Read-Shockley, and the BRK model. Although we use different energy models, the underlying physics in the simulations is the same: (1) the driving force in each case is the same (minimization of the total GB energy), and (2) the GBs move according to the same law (e.g. $v = \kappa$). To make quantitative comparisons, we performed grain growth simulations using all three models for every microstructure. For the isotropic model, all GBs were assigned the same energy regardless of their misorientation and GB normal. The other two energy models are described in detail below.

#### *2.2.1. Read-Shockley*

The Read-Shockley model [41] has been used extensively in previous simulations of anisotropic grain growth [25–30, 32]. It takes into account the GB misorientation but ignores the GB normal. It is

accurate for low angle misorientations, but it does not effectively predict the energy of high-angle misorientations [8].

In our simulations, we used the same form of the Read-Shockley function employed by Elsey [25]:

$$\gamma_{ij} = \begin{cases} \gamma_{\min} + (1-\gamma_{\min}) \frac{|\alpha_{ij}|}{\alpha_{\max}} \left[1 - \log\left(\frac{|\alpha_{ij}|}{\alpha_{\max}}\right)\right], & \text{if } |\alpha_{ij}| \leq \alpha_{\max} \\ 1, & \text{if } |\alpha_{ij}| > \alpha_{\max} \end{cases} \tag{10}$$

where $\alpha_{ij}$ is the misorientation angle between the $i$-th and $j$-th grains, and the value $\gamma_{\min}$ was 0.1 according to [25]. $\alpha_{\max}$ is the low-energy threshold of the RS model and controls the population of low-energy GBs. In computational studies, it is common to use a low-energy threshold in the RS model that is larger than the low-angle threshold [9, 13, 25, 29]. In the present work, the purpose of such a choice is to ensure that there is a non-negligible fraction of low-energy GBs, which would otherwise be artificially suppressed as a result of the uncorrelated assignment of grain orientations. In our simulations $\alpha_{\max} = 30°$, consistent with other works (c.f. [9, 13, 25, 29]).

#### *2.2.2. BRK model*

The energy model developed by Bulatov, Reed, and Kumar [44] is an interpolation function for GB energy in face-centered cubic metals that considers all five crystallographic degrees of freedom. Their approach was to model GB energy as a continuous function that depends on five crystallographic parameters and that any GB energy can be calculated by interpolating between known values from a dataset. Rather than using simple linear interpolation between data points (which would require a larger dataset than was available at the time to be accurate), they instead performed non-linear interpolation by incorporating prior information about the 5D crystallographic symmetry of the GB character space together with an *ansatz* for the GB energy variation between certain high-symmetry GBs referred to as scaffolding points.

Along with the original BRK publication [44], a MATLAB program was provided as supplementary data. This MATLAB program, called '`GB5DOF`', takes two rotation matrices, `P` and `Q`, as an input. The orientations of 2 grains that form a GB and the GB normal between them are defined by these rotation matrices. In this work, we employed the BRK function by means of the '`GB5DOF`' MATLAB routine to calculate the GB energies of each voxel that is part of a GB during every time step of the simulation.

### *2.3. Grain boundary normal calculation*

The GB normal and the misorientation define a GB. We need all five parameters to calculate the GB energies of each GB in the microstructure during the fully anisotropic simulations. As the level set method performs the convolution in the Fourier space, it was necessary to calculate the GB normal of every GB voxel in the microstructure.

A common method to obtain GB normals from voxelized microstructures is first to create a surface mesh of the GB network and then calculate the normal of each facet in that mesh. While there are software programs such as Dream3D [58] (which uses the 'marching cubes method' [59]) that can accomplish this, the resulting mesh is stair-stepped, and post-processing is required to obtain a smooth mesh. Available Hierarchical [60] or Laplacian [61] smoothing algorithms can improve the quality of the resulting mesh. However, it is possible to over- or under-smooth depending on the number of iterations. More importantly, meshing the GB network at each time step is computationally expensive.

An alternative approach, which we employed in this work, involves the calculation of GB normals directly from the voxelized microstructure via a method developed by Liberman et al. based on first-order Cartesian moments [62]. The method is based on the equation for finding general Cartesian moments of order $n$:

$$M_{abc}(\mathbf{r}) = \sum_{(i,j,k)\in S} w(\mathbf{r})\, x_i^a y_j^b z_k^c f(\mathbf{r}) \tag{11}$$

where $\mathbf{r} = [x_i, y_j, z_k]^\intercal$ is the position in the volume $S$ (voxelized 3D microstructure), and $w(\mathbf{r})$ is a weighting function that depends on the position. In this application, the weight is 1 for every point inside $S$. The order of a moment is given by $n = a + b + c$, and $f(\mathbf{r})$ is an indicator function that can take the values 1 or 0 depending on

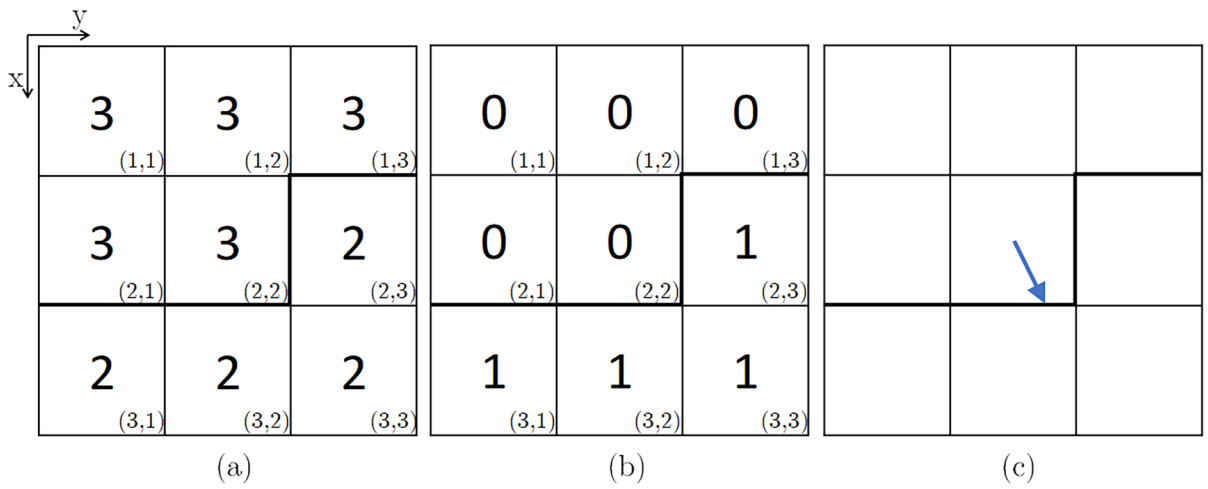


Figure 2: Steps in determining the GB normal for voxel in position (2,2). (a) Voxelized 2D image, grain IDs in the center, and location of the voxels in the right bottom. (b) Values of the indicator function, $f(\mathbf{r})$, generated at the voxel in position (2,2). (c) Grain boundary (thick black line) and calculated normal vector (blue arrow) for voxel in position (2,2).

whether the particular point belongs to a grain we are interested in or not.

As an example, consider the 2D microstructure in Fig. 2, composed of a $3\times3$ grid of voxels. Fig. 2a shows the voxel grain IDs (indicating which grain each voxel belongs to) in the center of each square and the position in the bottom-right corner. In this example, we have grain 2 and grain 3. These two grains form a GB (thick black line). Consider the calculation of the GB normal for the voxel in position (2,2). We begin by calculating the binary indicator function for this voxel. We obtain the IDs of the neighboring voxels, then all voxels with the same grain ID as the voxel in position (2,2) will be assigned a value of 0, while the voxels with the IDs of a neighbor grain will be assigned a value of 1, as illustrated in Fig. 2b.

In our simulations, there is an equal number of voxels in every direction and each voxel is a cube, meaning that the grid spacing is the same in every direction. Under these conditions the vector $\mathbf{r}$ is defined as:

$$\mathbf{r} = [x_i, y_j, z_k]^\intercal = [i\Delta x, j\Delta y, k\Delta z]^\intercal \tag{12}$$

where $\Delta x$, $\Delta y$, and $\Delta z$ represent the grid spacing.

After obtaining the value of the indicator function for each voxel, we calculate the components of the GB normal using the gradient of the indicator function [63] and the first-order moment with the following formulation of Eq. 11 (complete derivation provided in [62]):

$$\begin{aligned} M_{100}(\mathbf{r}) &= \frac{1}{\Delta x}\sum_i w(\mathbf{r})\, f(\mathbf{r})\, i \\ M_{010}(\mathbf{r}) &= \frac{1}{\Delta y}\sum_j w(\mathbf{r})\, f(\mathbf{r})\, j \\ M_{001}(\mathbf{r}) &= \frac{1}{\Delta z}\sum_k w(\mathbf{r})\, f(\mathbf{r})\, k \end{aligned} \tag{13}$$

The GB normal in the sample reference frame, $S$, is then obtained as

$$\mathbf{n}^S(\mathbf{r}) = [M_{100}(\mathbf{r})\,, M_{010}(\mathbf{r})\,, M_{001}(\mathbf{r})]^\intercal \tag{14}$$

Finally, the GB normal is expressed in the crystal reference frame of one of the incident grains according to

$$\mathbf{n}^i(\mathbf{r}) = g_i^{-1}\mathbf{n}^S(\mathbf{r}) \tag{15}$$

### *2.4. Validation examples*

Before performing the large-scale simulations, we verified that the implementation of the BRK function on the level set method was successful. Validation of the level set method itself was performed in [25]. In this section, we provide validation examples of our implementation of the BRK function (including GB normal calculation).

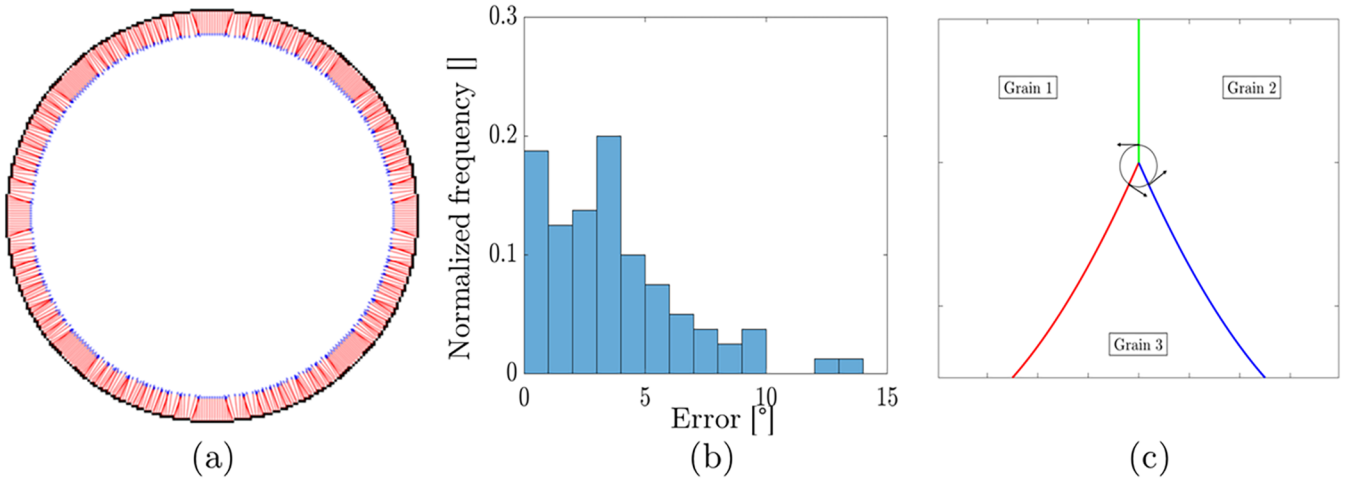


Figure 3: (a) Interface normals (red arrows) of a voxelized circular interface (black voxels) calculated using the first-order Cartesian moment approach [62]. (b) Distribution of errors. (c) Example of calculated GB normals around triple junctions.

#### *2.4.1. GB normal validation*

In Fig. 3, we show the results of a simple test of the method for a voxelized circular interface. In this example, the circle has a radius of 45 voxels in a $128 \times 128$ grid. The interface normal for each interface voxel was computed using the first-order Cartesian moment approach. As the voxelized microstructure is an approximation of the true underlying microstructure, the resulting normals are also an approximation, but they show good agreement with the expected normals, and the calculation is very fast. Liberman et al. compared surface meshing and the Cartesian moment approach and found that the resulting normals agreed on average to within 3° [62]. For the test case shown here, the actual normal at each point along the interface is known analytically from the equation of a circle (so no meshing is required), and the distribution of errors is shown in Fig. 3b. We found the average error to be 3.15° and the maximum error to be 13.6°.

We followed the same procedure outlined in this example to identify GB voxels and calculate their respective GB normals for our large-scale grain growth simulations. We then assigned the local GB energy of each voxel from one of the GB energy models described in Section 2.2.

#### *2.4.2. GB normals at triple junctions*

The Cartesian moment method employed to calculate the normals described in Section 2.3 works for voxels that belong to a GB. However, where three GBs meet at a triple junction, a GB normal is technically undefined. To assign normals and compute GB energies for voxels adjacent to a triple junction, we define a small exclusion zone of a fixed radius (5 voxels) surrounding the triple junction. GB voxels within the exclusion zone are assigned the normal of the first voxel along the corresponding GB that falls outside of the exclusion zone.

For example, Fig. 3c shows a triple junction constructed using known analytical functions. $GB_{13}$ is the curve $y = x^2$, $GB_{23}$ is the curve $y = (x-5)^2$, and $GB_{12}$ is the line $x = 1$. The black circle illustrates the exclusion zone, and the black arrows indicate the normals of voxels at its limits (five voxels away from the triple junction). For validation, we compute the angular deviation of the normals computed in this fashion, relative to the known analytical normals at the triple junction. We find the error between the calculated normal and the analytical normal to be 3.5° degrees, which is comparable to the angular deviation reported in Section 2.4.1 for GB voxels far from triple junctions.

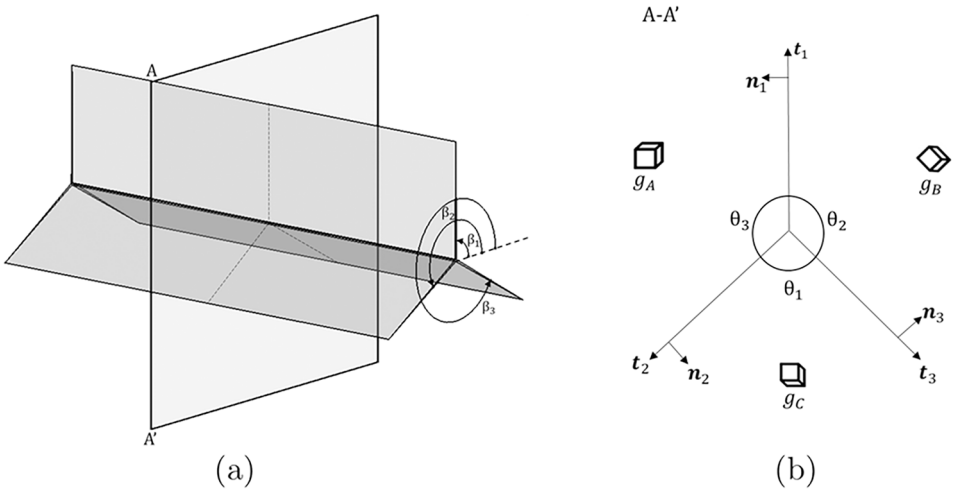


Figure 4: Triple junction geometry and parameters as employed in Eqs. 16 and 17. (a) 3D triple junction. (b) 2D orthogonal section of the 3D triple junction.

### *2.4.3. Grain boundary configuration at triple junctions*

While the level set algorithm developed by Esedoḡlu [27] satisfies the Herring equation [64], we performed additional validation to ensure that this is still the case when the effect of the GB normal and the BRK function are included.

The Herring equation describes the local equilibrium configuration of a GB triple junction. In [64], the Herring equation is expressed as

$$\sum_{i=1}^{3}\left(\gamma_i \mathbf{t}_i + \frac{\delta\gamma_i}{\delta\beta_i}\mathbf{n}_i\right) = \mathbf{0} \tag{16}$$

where $\mathbf{t}_i$ is the tangent vector and $\mathbf{n}_i$ is the normal vector. $\beta$ is the GB inclination angle, measured anti-clockwise with respect to an arbitrarily chosen reference direction (at a TJ). The quantities of this equation are shown in Fig. 4. In 3D, the triple junction is a line. However, the Herring condition applies at every point along the triple junction and at any orthogonal 2D section of that 3D line [65]. For the isotropic case, when the GB energies of the three GBs that form the TJ are equal, the dihedral angles are 120°. In the anisotropic case, for unequal GB energies, the angles are different.

The first component in Eq. 16 will move the junction to shorten the highest energy boundary. The second term, sometimes called the torque term, will cause changes in the respective GB inclinations to minimize the energy. The torque term is usually neglected because it is typically small for general GBs [64]. The simplified equation when neglecting the torque term is

$$\gamma_i \mathbf{t}_i + \gamma_j \mathbf{t}_j + \gamma_k \mathbf{t}_k = \mathbf{0}, \tag{17}$$

In this study, we *do not* neglect the torque term, and we here verify that the full Herring conditions are satisfied. In order to validate our implementation of the BRK function in the level-set-method, we performed simulations on a single TJ. We performed two simulations using the same initial microstructure and orientation. The first simulation used the Read-Shockley energy function, and the second used the BRK function. After performing the simulations, we calculated the normal and tangent vectors and the GB energies of the resulting TJ configuration. With these values, we calculated the left-hand side (LHS) of Eq. 16. The right-hand side (RHS) of the Herring equation is a vector of all zeros and therefore has a norm of zero. Previous authors verified that level-set simulations using the method of Esedoḡlu together with the Read-Shockley energy function satisfy the simplified Herring equation shown in Eq. 17 [27].

To verify that the BRK simulation satisfies the Herring conditions, we calculated the norm of the calculated LHS vector of Eq. 16, which should be close to zero. We repeated this for the Read-Shockley simulation in order to have these values

as a reference. We do not expect these values to be precisely zero, as the discretization of the microstructure could introduce some errors when calculating the normal and tangent vectors. However, the result should be close to zero.

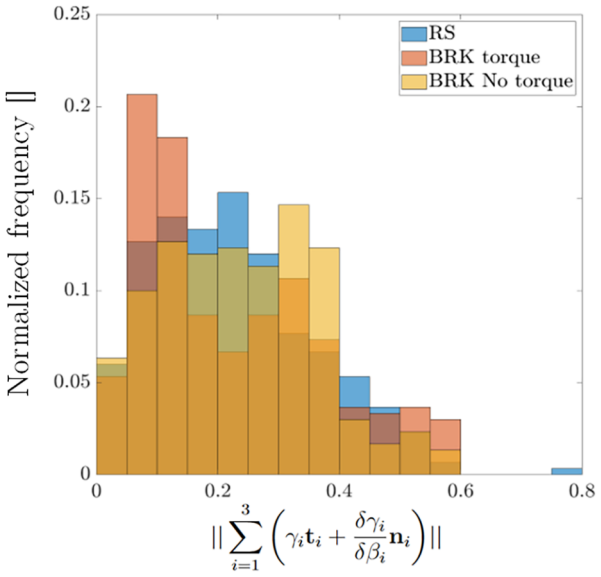


Figure 5: Distribution of magnitude of the LHS of the Herring equation (Eq. 16) when using the Read-Shockley vs. BRK GB energy functions.

Fig. 5 shows the results of 300 simulations using different initial orientations. The average value of the norm from the Read-Shockley simulations is 0.228, the average value of the norm from the BRK (neglecting the torque term) simulations is 0.239, and the average value of the norm from the BRK (including the torque term) simulations is 0.224. Since prior work confirmed that the present level-set method satisfies the Herring conditions when a Read-Shockley GB energy function is employed [27] and we find that the average error is of comparable magnitude when the fully anisotropic BRK energy function is employed (it is 1.8% lower), we conclude that the Herring conditions are also satisfied to the same level of accuracy in the present work. We note also that neglecting the torque term increases the error by about 6.7%, though the magnitude of the error remains small even in this case (a 6.7% increase in a very small error remains a small error).

Additionally, wetting is an effect that could happen at triple junctions when using level set methods. Wetting occurs when a new phase nucleates in an interphase between two existing phases. In our simulations, the conditions to prevent wetting are explicitly enforced, as suggested in [26]. When assigning a phase to each voxel of the microstructure, we restrict that only existing phases around the voxel are considered.

### *2.5. Experimental design*

Table 1 summarizes the five simulations that we performed. We used the same initial microstructure (i.e. there was one initial microstructure template for random texture and another for fiber texture) for each GB energy function in order to make quantitative comparisons on a grain-by-grain basis.

Table 1: Summary of simulations parameters for each of the 5 different simulations performed.

| Initial Texture | N/A | Random | | Fiber | |
|---|---|---|---|---|---|
| Energy function | Isotropic | RS | BRK | RS | BRK |
| Initial # of Grains | 7500 | 7500 | 7500 | 7500 | 7500 |
| Final # of Grains | 401 | 400 | 418 | 416 | 425 |

## 3. Results

Fig. 1c-e shows the final microstructure obtained from the random texture simulations when less than 5% of the initial grains remained for the isotropic, Read-Shockley, and BRK simulations, respectively. Of the less than 500 grains that remained, the three simulations share 75% of the same grains; the other 25% are grains that survive in only one or two of the simulations. Thus a significant fraction of the microstructure differs when using different GB energy models.

Moreover, even for the 75% of grains that survived in all three simulations, we find that the grain morphology (shape, dihedral angles at TJs, etc.) varies significantly depending on the employed GB energy model. Such effects of GB energy anisotropy on the morphology and evolution of individual grains have been observed in experimental grain growth studies [66]. The following subsections detail the similarities and differences between the microstructures using various structure metrics and microstructural statistics across GB energy models and initial crystallographic textures.

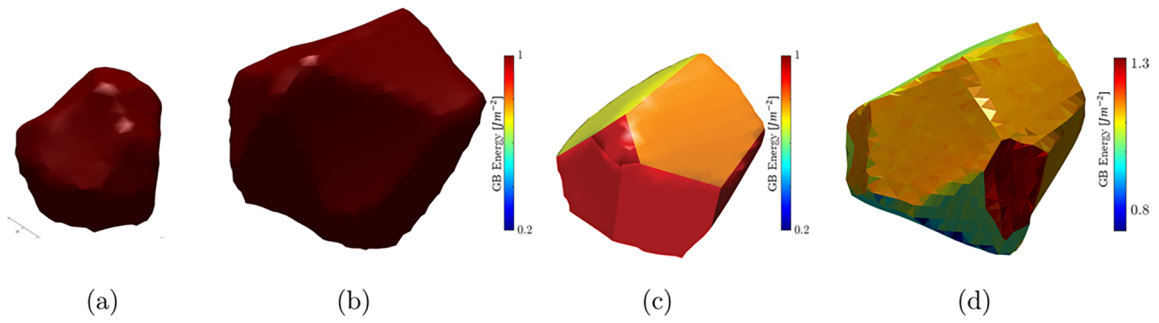


Figure 6: Evolution of an individual grain. (a) Grain from the random textured initial microstructure. Same grain after the microstructure has evolved for 100 time-steps under (b) Isotropic, (c) Read-Shockley, and (d) BRK simulations. Grains colored by GB energy.

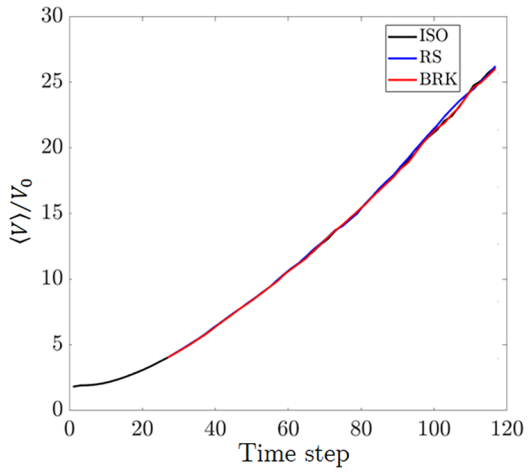


Figure 7: Normalized grain volume vs. time step. Initial transient (first $\sim$ 25 time steps) corresponds to the initialization step of isotropic grain growth described in Section 2.1.1.

### *3.1. Morphology evolution*

Fig. 6 shows an individual grain from the random texture initial microstructure that survived in each of the three simulations using different GB energy functions. Fig. 6a shows the initial grain before the simulation started. In Fig. 6b-d, we see how this grain evolved into different grain morphologies depending on the GB energy function used in the simulation. While this grain grows to larger than the average grain size under isotropic conditions, the grain did not grow as much when using anisotropic energies. In addition, we can observe how the grain has different shapes and different GBs depending on the energy function.

Table 1 shows the number of remaining grains when using different energy functions and starting with different initial textures. Kim et al. [17] reported that when using an energy function that considers the misorientation and the plane normals, the number of remaining grains is a little larger than when using isotropic conditions. In agreement with those results, the kinetics of our BRK simulations appear to be slightly slower than the Read-Shockley and isotropic simulations (i.e. there are more grains in the final BRK microstructures, indicating that the coarsening process has not proceeded as far as in the isotropic and Read-Shockley simulations which omit the dependence on GB normal), though we cannot quantitatively compare the rates.

### *3.2. Normalized grain growth and grain size distribution*

Fig. 7 shows the mean grain volume over the course of the simulations, normalized by the initial volume. The simulations seem to all reach steady state (the plot becomes linear) after about 15-20 time steps. There also appears to be no significant difference between the way the average volume evolves using different GB energy functions. This could be a manifestation of the fact that in this version of Esedoḡlu's MATLAB implementation of the level-set method $v = \kappa$ which implies that $M\gamma = 1$. As a result, one limitation of the simulations is that they do not capture independent mobility effects (though, as noted earlier the effect of mobility is expected to be small compared to the effect of the GB energy). Nevertheless, the different GB energy functions do result in different dihedral angles and grain morphologies, and it is therefore notable that

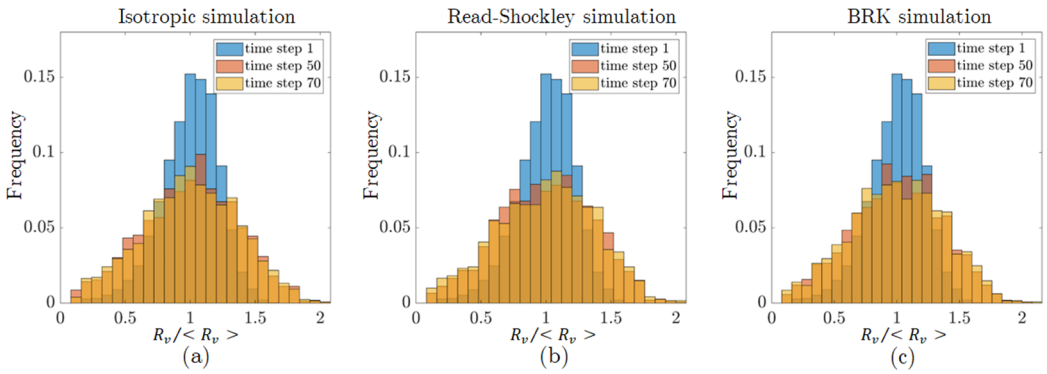


Figure 8: Normalized grain size distribution of 3 different times-steps when starting with a random texture microstructure for (a) Isotropic, (b) Read-Shockley and (c) BRK simulations. $R_v$ is the spherical equivalent grain radius, and $\langle R_v \rangle$ is the average spherical equivalent grain radius.

the evolution of the average grain volume seems to be largely independent of these morphological differences.

Figure 8 shows the grain size distribution of the initial microstructure and two later time-steps. We can see that the distribution broadens in the later time-steps, and the microstructure seems to reach self-similarity (the distributions at time step 50 and 70 are nearly identical). To verify this, we ran a two-sample Kolmogorov-Smirnov test for the random texture (uniform ODF) simulations to evaluate if the grain size distributions for the later time-steps come from the same distribution. For each case, the results confirm that the distributions are statistically indistinguishable with $p$-values of 0.57; 0.76 and 0.63 for the isotropic, Read-Shockley and BRK simulations, respectively. The grain size distributions for the fiber texture simulations exhibited similar results and self-similarity was also observed.

### *3.3. Grain boundary energy distribution*

The GB energy function directly impacts the evolution of the grain boundary energy distribution (GBED). Fig. 9 shows the GBED of the initial and final microstructure for the simulations using the Read-Shockley function and the simulations using the BRK function (the isotropic GBED is uniform by definition at all times). When the initial microstructure has random texture, the GBED for both the Read-Shockley simulation and BRK simulations (while different from each other) are very similar between their respective initial and final states. Most of the GB energies are in the interval $0.9-1\,\mathrm{J/m^2}$ for the Read-Shockley simulation and $1-1.4\,\mathrm{J/m^2}$ for the BRK simulation, respectively. In both simulations, there are very few GBs with energies in the interval $0.1-0.5\,\mathrm{J/m^2}$. On the other hand, when the initial microstructure has a fiber texture (Fig. 9c-d), the GBED exhibits a broader range of values—including a significant proportion of low-energy GBs—and as the microstructure evolves the population of low-energy GBs increases for both the Read-Shockley and BRK simulations. Thus, the initial texture appears to have a qualitative influence on the evolution of the GBED.

### *3.4. Orientation distribution function*

In Fig. 10a-b, we present (001) and (111) pole figure representations of the ODF of the initial and final microstructure for the BRK simulation. The ODF is essentially uniform in both cases. For the fiber texture simulations, Fig. 10c-d shows that the ODF changes in a non-negligible way. The initial ODF shows that the [001] directions are aligned with the sample $Z$-axis and that there is an equal probability for any rotation having [001] parallel to the $Z$-axis As the microstructure evolves during grain growth, modest peaks emerge, indicating preferred orientations. The final ODF appears somewhat like a rotated cube texture mixed with a fiber texture.

The fact that there is no change to the ODF

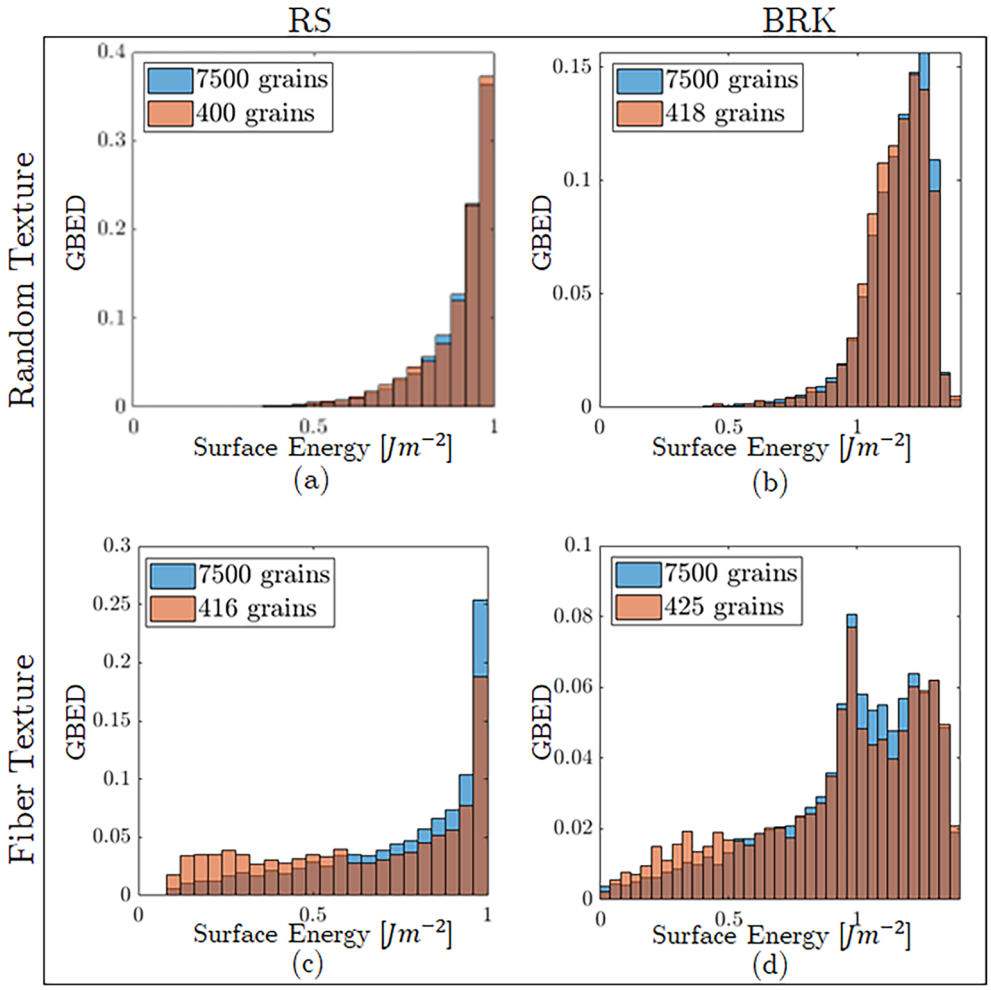


Figure 9: GB Energy Distribution of the initial and final microstructure of the simulations when initial random texture is assigned for the (a) Read-Shockley and (b) BRK simulations; and when initial fiber texture is assigned for the (c) Read-Shockley and (d) BRK simulations.

when it is initially random suggests that the ODF remains self-similar during evolution and that the microstructure doesn't have the opportunity (i.e. there is no kinematic pathway) to minimize its energy by mechanisms that produce preferred orientations.

### *3.5. Misorientation distribution function*

Fig. 11 shows the misorientation distribution function (MDF) for the simulations. As expected for random texture (Fig. 11a-c) in the cubic system, the initial distribution is very close to the Mackenzie distribution [69]. The MDFs of the simulations' final microstructures that start with random texture do not change significantly for any of the three GB energy functions. As observed in [25] and [17], when assigning random texture, the evolution of the MDF is very slow as there are very few low-energy boundaries to start with. As a result, it is probably required to evolve the simulation for long times to see significant changes. However, if the simulation is run for a long time, most grains would disappear. Therefore, it is unlikely that one would ever be able see a change in the shape of the MDF for this scenario.

In contrast to the random texture simulations, the results of the MDF for the simulations using an initial microstructure with fiber texture are very different. Fig. 11d-f shows how the MDF of the initial microstructure is a uniform distribution for the isotropic, Read-Shockley, and BRK simulations. In this case, the final microstructure of the isotropic

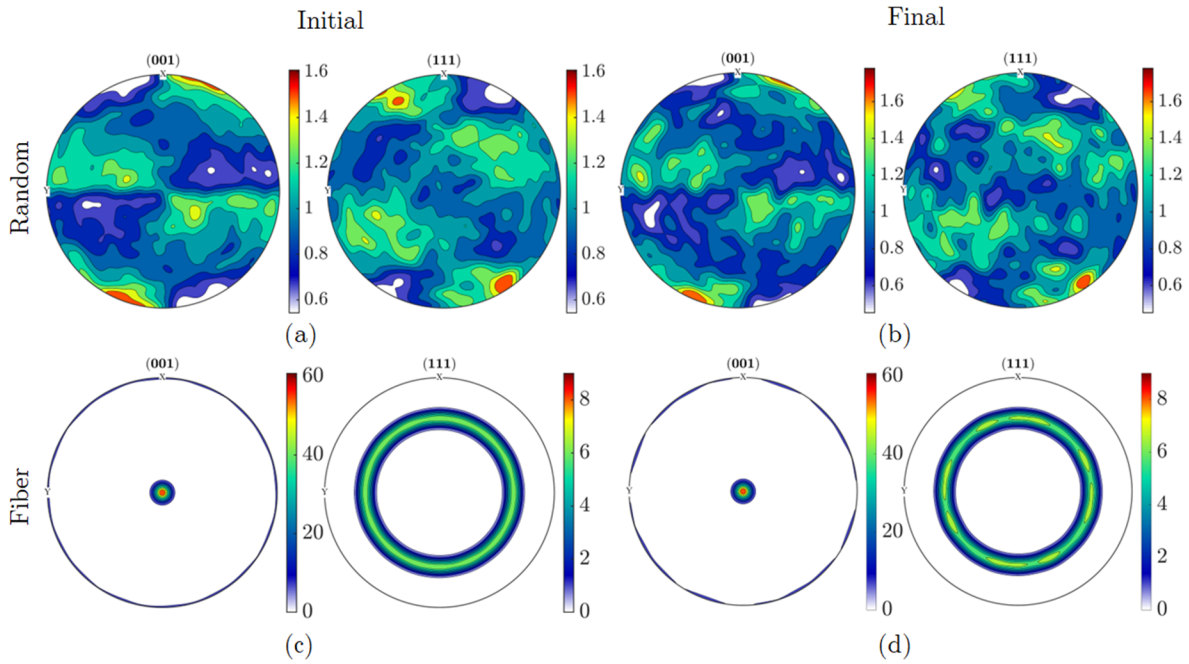


Figure 10: Orientation Distribution Function of the (a) initial and (b) final microstructure of the BRK simulations with initial random texture and the (c) initial and (d) final microstructure of the BRK simulations with initial fiber texture. Pole figures were constructed using MTEX [55].

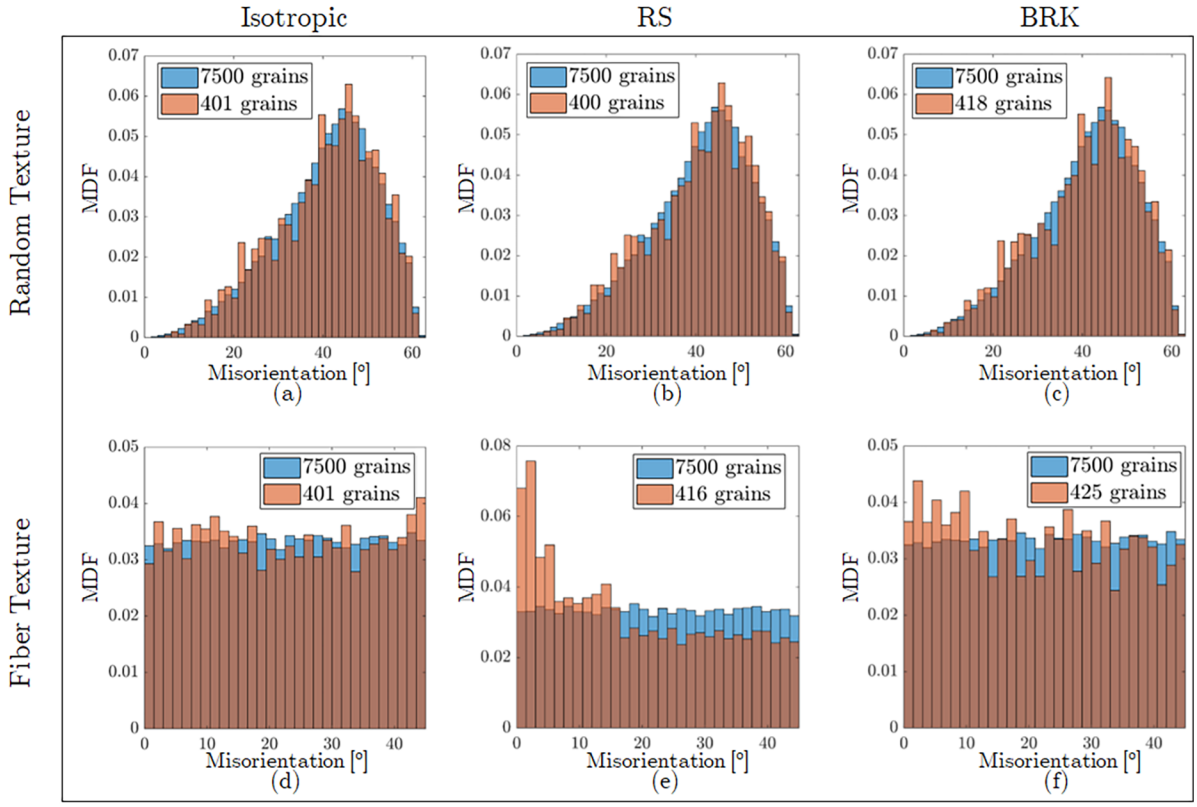


Figure 11: Misorientation Distribution Function of the initial and final microstructure of the simulations when initial random texture is assigned for the (a) Isotropic, (b) Read-Shockley, and (c) BRK simulations; and when initial fiber texture is assigned for the (d) Isotropic, (e) Read-Shockley, and (f) BRK simulations.

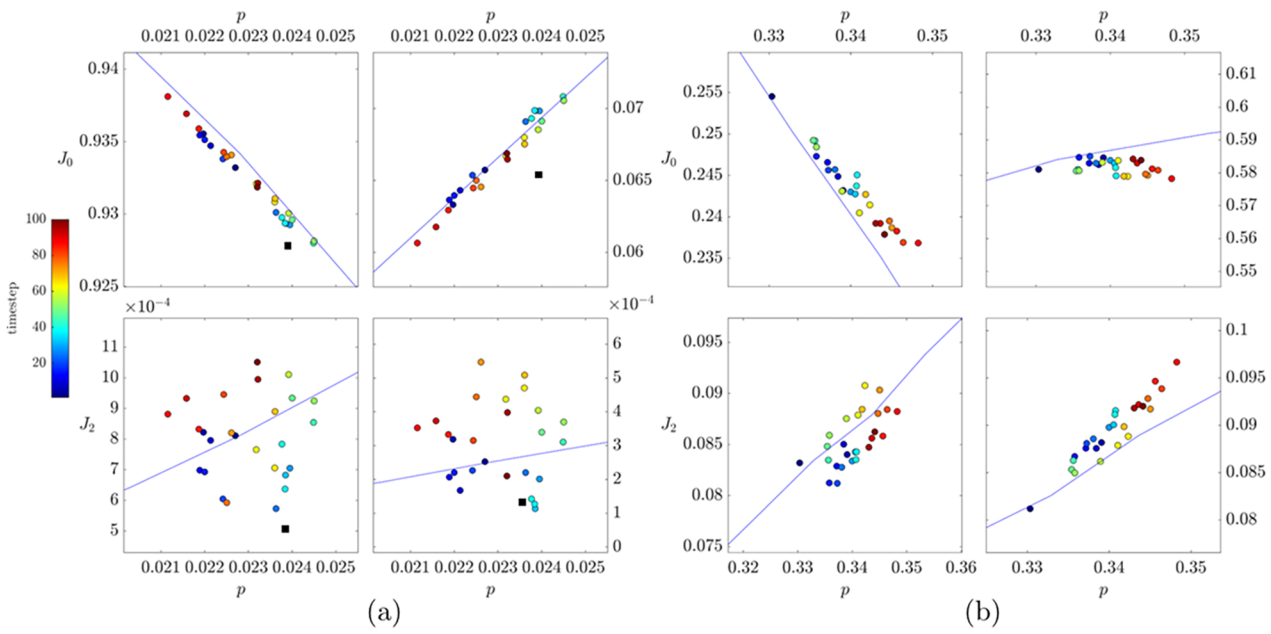


Figure 12: Triple Junction Distribution evolution of the microstructures from the grain growth simulation using the BRK GB energy function when the initial microstructure has initial (a) random and (b) fiber texture. Blue lines show the uncorrelated TJD for random and fiber texture, respectively. Black squares in (a) are TJD from experimental data [67, 68] with LAGB threshold of $\theta = 15°$.

simulation remains uniform. However, the distribution shifts toward lower misorientations in the Read-Shockley simulation and the BRK simulation. This result is consistent with the GBED results that show how the distribution moves towards low energy boundaries for the fiber texture case.

### *3.6. Triple junction distribution*

The triple junction fractions, denoted $(J_i)$, indicate the fraction of TJs in the microstructure coordinated by $i$ low-angle GBs (LAGBs). The values $[J_0, J_1, J_2, J_3]$ are sometimes referred to as the TJ distribution (TJD), and the evolution of the TJD is plotted in Fig. 12 for the BRK simulations. In Fig. 12, $p$ is the length-fraction of LAGBs, where the traditional 15° threshold is used. We note that the range of $p$ values in the random texture case is small ($0.0212 - 0.0245$ over the course of the grain growth simulations). The TJs are predominantly $J_0$-type at the beginning of the simulation. As the microstructure evolves it seems that there is no significant change in the fraction of LAGBs and no clear trend in the variation of the $J_i$. In addition, the TJ fractions are very close to the uncorrelated TJD (blue lines) [70–72].

Similarly, the evolution of the TJD for the fiber texture grain growth simulation in Fig. 12b does not deviate from the uncorrelated TJD. However, in this case, the increase in the fraction of LAGBs, $p$, as the microstructure evolves is appreciable, roughly 6 %. In addition, there is a trend of decreasing $J_0$ and increasing $J_2$ and $J_3$ as the system evolves, while $J_1$ remains approximately constant. The decrease in $J_0$ and increase in $J_2/J_3$ indicate an increase in the connectivity of LAGBs and a reduction in the connectivity of high-angle GBs (HAGBs). Finally, we analyze the evolution of the GB network topological order parameters: $\chi$—which indicates the tendency of LAGBs to form compact or elongated clusters—and $\sigma$—which indicates the tendency for LAGBs and HAGBs to mix or phase separate [70]. In the initial microstructure $\chi \approx 0$, so there is no preference for compact vs. elongated clusters. On the other hand, $\sigma \approx 0.32$, indicating a preference for phase separation of the LAGBs and HAGBs. As the microstructure evolves, $\sigma$ does not change significantly. However, $\chi$ increases slightly to $\sigma \approx 0.35$, indicating that the LAGB clusters appear to become more elongated.

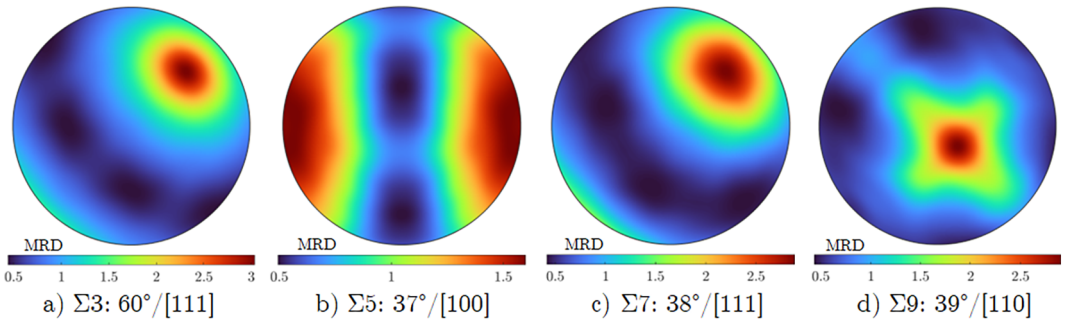


Figure 13: GBCD for (a) Σ3, (b) Σ5, (c) Σ7 and (d) Σ9 of the fully anisotropic BRK simulations. The [001] direction is normal to the page and [100] direction is horizontal and to the right. The number of observations (voxels) in the microstructure for GBs exhibiting Σ3, Σ5, Σ7 and Σ9 disorientations were 8450, 5521, 4634 and 6163, respectively. Figures were constructed using MTEX [55].

In Appendix A, we show the TJD of the isotropic and Read-Shockley simulations. For the isotropic simulations, as expected, there is essentially no variation of LAGBs. The Read-Shockley simulations reproduce the same qualitative trends observed here for the BRK GB energy function, for both the initial random texture and initial fiber texture.

### *3.7. Grain boundary character distribution (GBCD)*

In this section, we present the results of the GBCD for the resulting microstructures from the BRK simulations that had random texture. As the initial microstructure of the simulations started with fully random orientations, the distributions of plane normals for the initial time steps are essentially uniform and are not shown here. However, the GBCD changed significantly during the fully anisotropic (BRK) grain growth simulations, and we present the GBCD for several low-Σ misorientations after the microstructure reached steady-state in Fig. 13.

The GBCDs obtained from the fully anisotropic BRK simulations are similar to experimental GBCD observations [8, 73]. In contrast, the GBCDs for the isotropic and Read-Shockley simulations remained essentially random throughout the simulations, which is expected due to the fact that these energy functions do not consider the influence of the plane normal.

By construction, all misorientations in the fiber texture simulations have a [001] rotation axis, so only the GBCD of the Σ5 is relevant for these simulations. We found that the GBCD for the Σ5 misorientations from the BRK fiber texture simulations (not shown) was similar to the Σ5 GBCD for the BRK random texture simulations in the final microstructures.

The favorable comparison between the GBCDs observed for the fully anisotropic BRK simulations and those for experimental measurements in the literature, together with the absence of preferred GB normals in the Read-Shockley and isotropic simulations, suggest that the microstructures produced by the fully-anisotropic BRK simulations are more faithful to experimental microstructures and should be useful surrogates to study fully anisotropic grain growth.

## 4. Discussion

As is apparent from the foregoing results, for an initial random texture, every statistical microstructure descriptor remains essentially constant during the evolution, while nearly all of the descriptors change for an initial fiber texture. In addition, apart from the GBCDs, the microstructure statistics for the Read-Shockely and BRK simulations are at least qualitatively similar to one another. In this section, we explore possible explanations for these observations.

To understand how the initial texture influences the evolution of the GBED, recall that the system can minimize its energy by following one or more of the following four mechanisms:

1. Coarsening (reducing the total GB area).
2. Replacing high-energy GBs with low-energy GBs by the formation of low-energy GBs when a grain disappears.
3. Expanding the size of low-energy GBs at the expense of high-energy GBs by the motion of TJs.
4. Changing GB character through reorientation of the GB plane[2].

Mechanism 1 applies to all of our simulations (isotropic, read-Shockley and BRK). Regardless of the GB energy function employed, as the average grain size increases, the GB area decreases, and consequently, the total GB energy is reduced.

Mechanisms 2 and 3 are only relevant for the partially- and fully-anisotropic cases (Read-Shockley and BRK, respectively). During the anisotropic simulations, a shift toward LAGB misorientations was expected. We see this trend in the fiber texture simulations. However, the MDF and GBED for the simulations that started with a random texture did not change significantly.

The contribution of mechanism 2 to the variation of the various statistical descriptors is practically zero. A new GB is created when a grain disappears, and two grains (that did not share a boundary before) become neighbors. If these newly formed GBs tend to be LAGBs, the microstructure will reduce its energy by this mechanism, and we would see this difference in the MDF and GBED. However, for both the initial random and fiber textures, the probability that the newly created GBs at each time step happen to be LAGBs is very small. In fact, the newly created GBs show a similar MDF to the initial microstructure (see Fig. 14). Therefore, the newly created GBs are essentially sampled form the same distribution as the initial MDF and GBED so these statistical microstructure descriptors remain unchanged. This is at least partially due to the fact that these microstructures did not exhibit any spatial correlations in grain orientation (the orientations were assigned uniformly at random). It is conceivable that if certain types of strong spatial correlations in grain orientation exist, the distribution of newly created GBs could differ from the parent distribution and one might observe microstructural changes by this mechanism.

The lack of change in the random texture simulations could also be explained by the fact that the percentage of LAGBs in the initial microstructure is extremely low. When grain growth starts in a situation where most GBs are HAGBs, as seen in the random texture cases, the few initial LAGBs will probably be preserved (mechanism 3) as the microstructure coarsens. This implies that the fraction of LAGBs is actually increasing. However, because the proportion of LAGBs is negligible compared to that of the HAGBs, the change is insignificant, and the final MDF, GBED, ODF and TJD are indistinguishable from the initial distributions. By way of illustration, in the present simulations, the initial fraction of LAGBs for the initial random textured microstructure was 0.018. At the end of the simulation, the fraction of LAGBs increased by 17 % to 0.021, which, in spite of representing a large percent increase, is still practically indistinguishable from the initial fraction.

In contrast, for the fiber texture cases there is a higher proportion of LAGBs in the initial microstructure. As this initial proportion of LAGBs increases during grain growth it has a noticeable impact on the MDF, GBED and TJD. Continuing the previous comparison, the initial fraction of LAGBs for the initial fiber textured microstructure was 0.321. In this case, the LAGB fraction increased by 22 % to 0.392. Though a similar percent increase to the random textured simulations (22 % compared to 17 %), this represents a much larger and more noticeable absolute increase (0.071 compared to 0.003). Thus, it is possible that both the random and fiber texture simulations benefit from mechanisms 2 and 3, but the effect is only observable for the fiber textured microstructures because they have a significant fraction of LAGBs to begin with. Similar observations have been made in [17, 25].

Mechanism 4 is only available to the BRK simulations as these do not neglect the influence of the GB plane normal. Considering the influence of the GB energy anisotropy for different GB nor-

[2]GB character can also change by grain rotation under certain conditions [74–76].

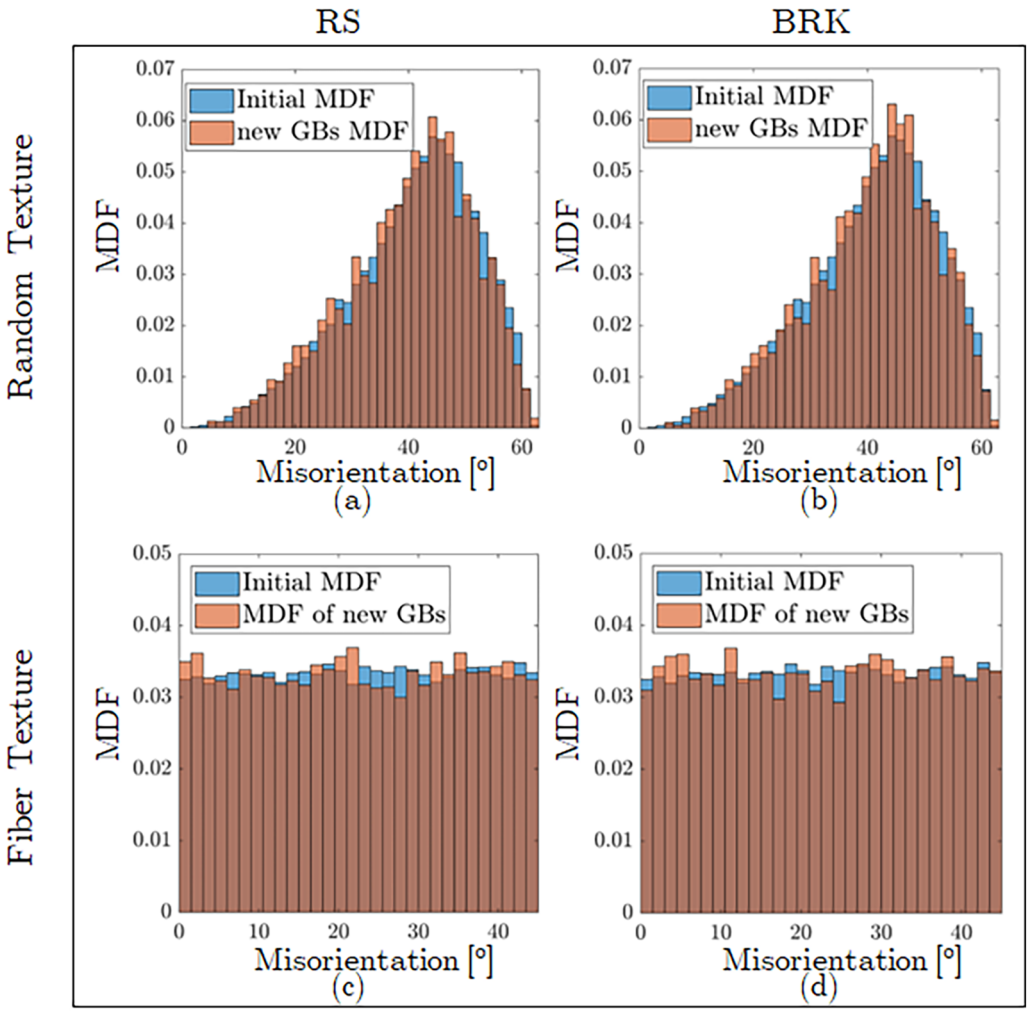


Figure 14: MDF of the initial microstructure and MDF of the GBs created at different time-steps for (a) random texture – Read-Shockley simulation, (b) random texture – BRK simulation, (c) fiber texture – Read-Shockley simulation and (d) fiber texture – BRK simulation.

mals should open up another path by which GBs can reduce their energies by reorientation of the GB plane. However, the shape of the BRK function is such that, for most misorientations, changing the normal only changes the GB energy by a small percentage (cf. [44]).

Finally, we compare the contribution of each mechanism to the reduction of the total interfacial energy of the microstructures from the BRK simulations. If the energy had been isotropic the percent reduction in energy would have been entirely due to the percent reduction in GB *area* which was 60.37% for the random texture case and 60.09% for the fiber texture case. The total reduction of *energy* for the BRK simulations was 62.72% for the random texture case and 64.78% for the fiber texture case. In the BRK simulations, the reduction is a combination of mechanisms 1, 3, and 4. If we assume that the contribution from mechanism 1 is the same as the percent reduction in GB area, we obtain the combined percent reduction from mechanisms 3 and 4 to be 2.35% and 4.69% for the random and fiber texture cases, respectively. Therefore, even though the system does take advantage of energy reductions via changing GB characters, as evidenced by the significant evolution of the GBCD, the amount that the total interfacial energy is reduced by this mechanism is small compared to how much it is reduced by coarsening. More details regarding the evolution of the total interfacial energy with time are provided in Appendix B.

This dominance of the purely geometrical coars-

ening effect may explain, at least in part, why many of the *spatially independent* macroscopic statistical descriptors (grain size distribution, GBED, MDF) evolved similarly—largely independent of the details of the underlying GB energy function. While the contribution of the GB energy anisotropy to the total reduction of interfacial energy is much smaller, it nevertheless has significant effects on the *spatially dependent* details of the microstructure evolution, including grain morphology and even which grains persist and which are eliminated from the microstructure.

## 5. Conclusion

In this work, we performed fully anisotropic grain growth simulations for 3D polycrystals with 7500 initial grains. We evaluated the effect of different grain boundary (GB) energy functions and initial crystallographic textures on microstructural evolution during grain growth. We considered isotropic, Read-Shockley, and fully anisotropic GB energy models; and initial random or fiber texture orientation distribution functions (ODFs). Our observations are summarized below:

1. Individual grains exhibited different morphological evolution (as well as disappearance or persistence) depending on the GB energy model employed. However, certain non-spatial statistical descriptors (grain size distribution, GBED, MDF) exhibited striking similarity independent of the GB energy model employed. This suggests that while the detailed microstructural evolution depends strongly on the GB energy function, many spatially independent statistical properties do not, and that statistical observations from simple isotropic simulations may be good approximations of fully anisotropic grain growth for some attributes of the microstructure (even when the detailed microstructural evolution is not).
2. The effect of the initial crystallographic texture is significant. When the initial texture is random, most statistical microstructural descriptors (GBED, MDF, ODF, TJD) remain essentially constant during grain growth. In contrast, when the initial crystallographic texture is a fiber texture, there are significant changes in all of the statistical microstructural descriptors. Moreover, the evolution is such that the statistics of the fiber textured microstructures do not simply evolve to resemble those of a random texture, but rather most of them evolve to become more and more *different* from it (e.g. the GBED, ODF, MDF, and TJD). This suggests that the evolutionary pathways of different initial microstructural states may diverge (or at least remain distinct) rather than converging.
3. The initial population of low energy boundaries impacts the apparent evolution of the GBED, MDF and the TJD. When there is a low population of low energy boundaries to begin with, there is not a significant change in this proportion at the end of the simulation. However, if there is a high population of low energy boundaries in the initial microstructure, the increase in that population will be more noticeable.
4. The system lowers its energy much more by coarsening than by changes induced by GB energy anisotropy. However, the GB energy anisotropy has a significant impact on the *spatially dependent* details of the microstructure.

## Acknowledgement

The material presented here is based upon work supported by the National Science Foundation under Grant No. 1654700. This work was supported in part through computational resources provided by Brigham Young University's Office of Research Computing.

## A. Appendix A

In this section, we present the results of the TJD evolution for the Read-Shockley and isotropic simulations. Fig. 15 shows that for the isotropic simulations the respective TJ fractions remain relatively constant and do not follow any trend during the simulation. This lack of change was expected because the MDF didn't change significantly for any of the isotropic simulations.

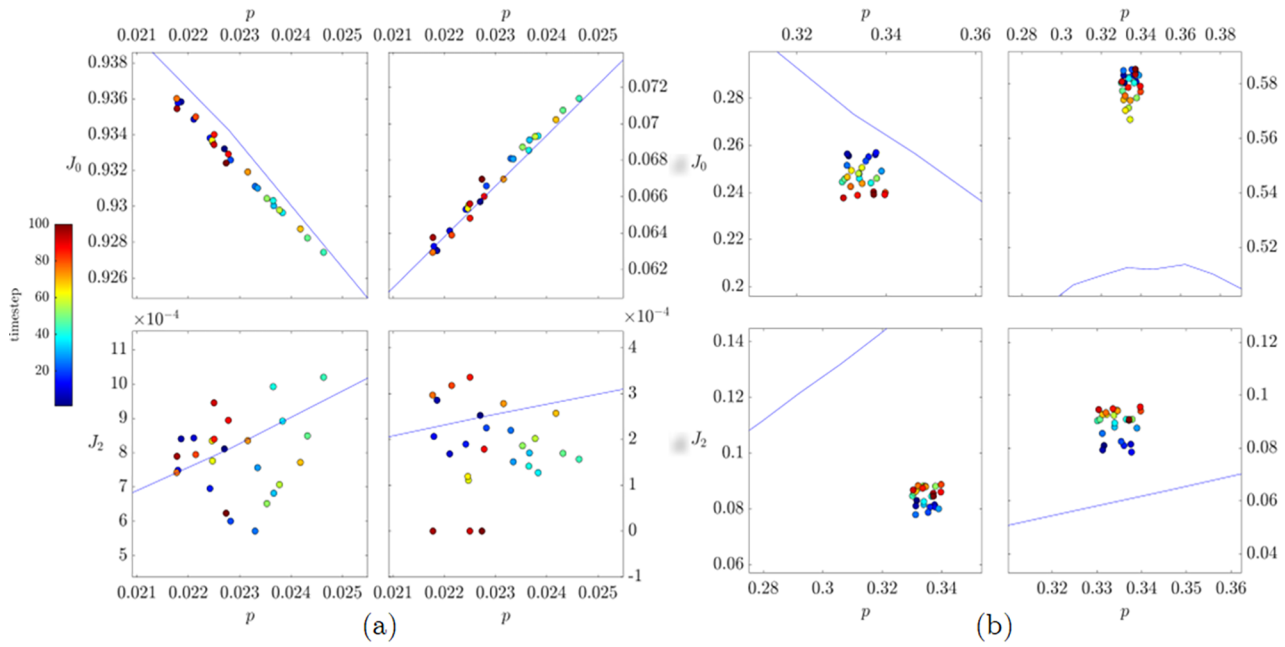


Figure 15: Triple Junction Distribution evolution of the microstructures from the grain growth simulation under isotropic GB energy conditions when the initial microstructure has initial (a) random and (b) fiber texture.

On the other hand, the TJD evolution for the Read-Shockley simulations, shown in Fig. 16, is qualitativly similar to the BRK simulations. In the random texture case, as most GBs are HAGBs (see the MDF in Fig. 11), most of the TJs are of type-0, and there are very few type-1,2, or 3 TJs. For the fiber texture case, which exhibits a higher fraction of LAGBs to begin with, there is a noticeable increase in the length-fraction of LAGBs, as well as an increase in $J_2$ and $J_3$.

## B. Appendix B

In this section, we present the results of the total interfacial energy evolution during the simulations for the different energy models. Fig. 17 shows the total energy vs. time steps for the isotropic, Read Shockley, and BRK simulations. The purpose of these plots is to show that the energy decays monotonically during the simulations. The three figures are for the random texture case. Similar trends were observed in the fiber texture case.

## 6. Data availability

The raw data required to reproduce these findings cannot be shared at this time as the data also forms part of an ongoing study. The processed data required to reproduce these findings cannot be shared at this time as the data also forms part of an ongoing study.

## References

[1] C. Tweed, B. Ralph, N. Hansen, The pinning by particles of low and high angle grain boundaries during grain growth, Acta metallurgica 32 (9) (1984) 1407–1414.

[2] J. W. Cahn, The impurity-drag effect in grain boundary motion, Acta metallurgica 10 (9) (1962) 789–798.

[3] M. Obstalecki, S. L. Wong, P. R. Dawson, M. P. Miller, Quantitative analysis of crystal scale deformation heterogeneity during cyclic plasticity using high-energy x-ray diffraction and finite-element simulation, Acta Materialia 75 (2014) 259–272.

[4] J. Oddershede, J. Sun, N. Gueninchault, F. Bachmann, H. Bale, C. Holzner, E. Lauridsen, Non-destructive characterization of polycrystalline materials in 3d by laboratory

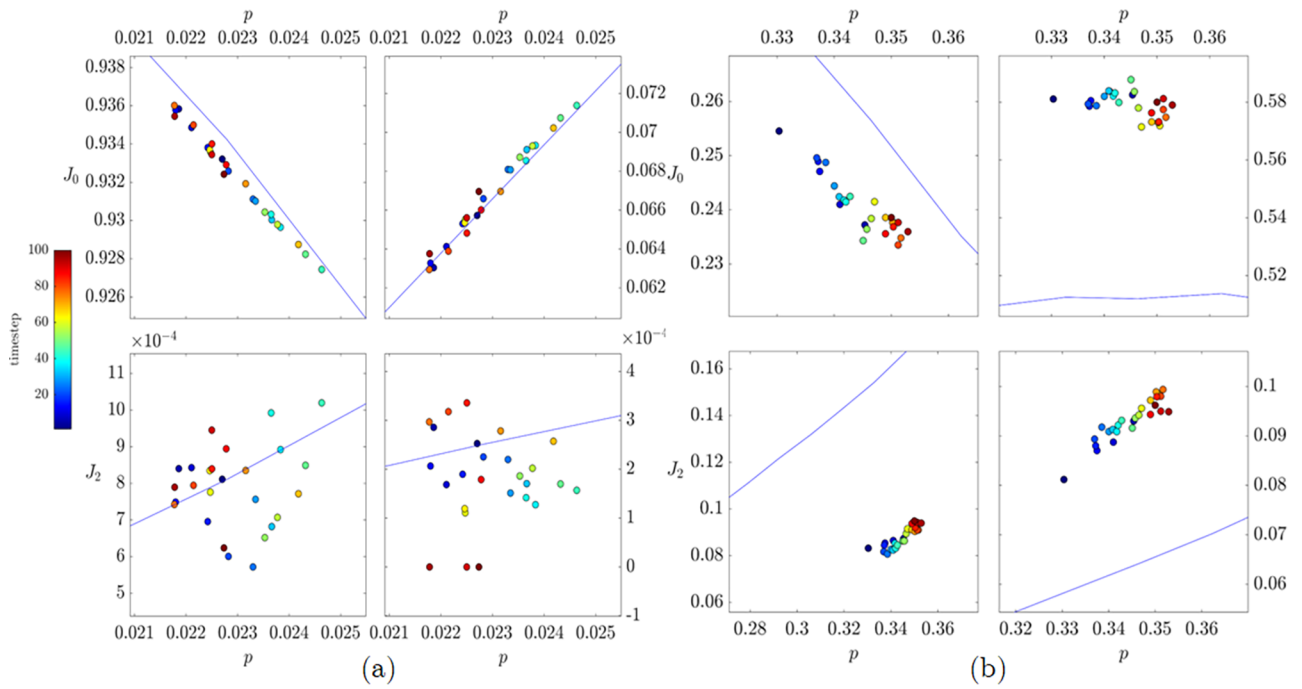


Figure 16: Triple Junction Distribution evolution of the microstructures from the grain growth simulation using the Read-Shockley GB energy conditions when the initial microstructure has initial (a) random and (b) fiber texture.

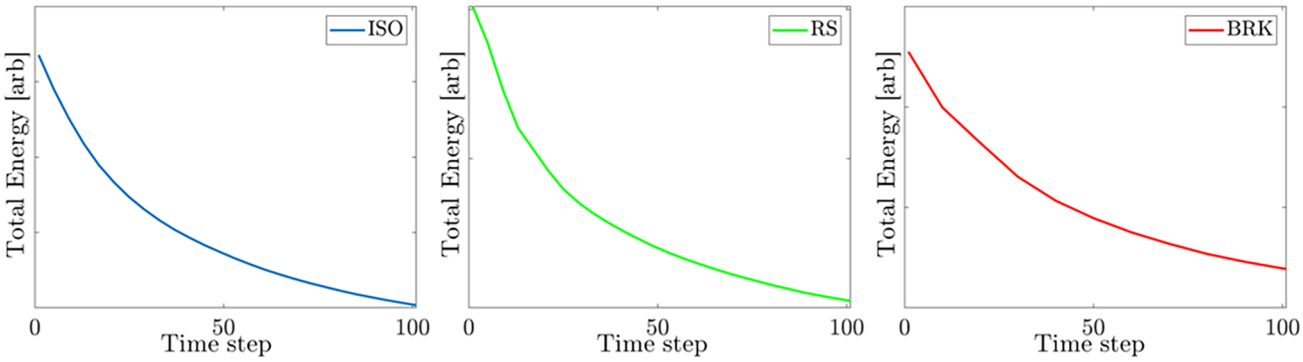


Figure 17: Total interfacial energy vs. time step for the isotropic, Read-Schockley, and BRK energy models, respectively.

diffraction contrast tomography, Integrating Materials and Manufacturing Innovation 8 (2) (2019) 217–225.

[5] A. J. Shahani, X. Xiao, E. M. Lauridsen, P. W. Voorhees, Characterization of metals in four dimensions, Materials Research Letters 8 (12) (2020) 462–476.

[6] A. Bhattacharya, Y. F. Shen, C. M. Hefferan, S. F. Li, J. Lind, R. M. Suter, C. E. Krill, G. S. Rohrer, Grain boundary velocity and curvature are not correlated in Ni polycrystals, Science 374 (6564) (2021) 189–193. doi:10.1126/science.abj3210.

[7] Z. Trautt, M. Upmanyu, Direct two-dimensional calculations of grain boundary stiffness, Scripta Materialia 52 (11) (2005) 1175–1179. doi:https://doi.org/10.1016/j.scriptamat.2004.12.033.
URL https://www.sciencedirect.com/science/article/pii/S135964620500014X

[8] G. S. Rohrer, Grain boundary energy

anisotropy: A review, Journal of Materials Science 46 (18) (2011) 5881–5895. doi:10.1007/s10853-011-5677-3.

[9] E. A. Holm, G. N. Hassold, M. A. Miodownik, On misorientation distribution evolution during anisotropic grain growth, Acta Materialia 49 (15) (2001) 2981–2991. doi:10.1016/S1359-6454(01)00207-5.

[10] D. Moldovan, D. Wolf, S. R. Phillpot, A. J. Haslam, Mesoscopic simulation of two-dimensional grain growth with anisotropic grain-boundary properties, Philosophical Magazine A: Physics of Condensed Matter, Structure, Defects and Mechanical Properties 82 (7) (2002) 1271–1297. doi:10.1080/01418610208235672.

[11] M. Upmanyu, G. Hassold, A. Kazaryan, E. Holm, Y. Wang, B. Patton, D. Srolovitz, Boundary Mobility and Energy Anisotropy Effects on Microstructural Evolution During Grain Growth, Interface Science 10 (2/3) (2002) 201–216. doi:10.1023/A:1015832431826.
URL http://link.springer.com/10.1023/A:1015832431826

[12] J. Gruber, D. C. George, A. P. Kuprat, G. S. Rohrer, A. D. Rollett, Effect of anisotropic grain boundary properties on grain boundary plane distributions during grain growth, Scripta Materialia 53 (3) (2005) 351–355. doi:10.1016/j.scriptamat.2005.04.004.

[13] J. Gruber, H. M. Miller, T. D. Hoffmann, G. S. Rohrer, A. D. Rollett, Misorientation texture development during grain growth. Part I: Simulation and experiment, Acta Materialia 57 (20) (2009) 6102–6112. doi:10.1016/j.actamat.2009.08.036.
URL http://dx.doi.org/10.1016/j.actamat.2009.08.036

[14] Y. Lan, D. Li, Y. Li, A mesoscale cellular automaton model for curvature-driven grain growth, Metallurgical and materials transactions B 37 (1) (2006) 119–129.

[15] N. Moelans, F. Wendler, B. Nestler, Comparative study of two phase-field models for grain growth, Computational Materials Science 46 (2) (2009) 479–490. doi:10.1016/j.commatsci.2009.03.037.
URL http://dx.doi.org/10.1016/j.commatsci.2009.03.037

[16] A. Mallick, S. Vedantam, Phase field study of the effect of grain boundary energy anisotropy on grain growth, Computational Materials Science 46 (1) (2009) 21–25. doi:10.1016/j.commatsci.2009.01.026.
URL http://dx.doi.org/10.1016/j.commatsci.2009.01.026

[17] H. K. Kim, S. G. Kim, W. Dong, I. Steinbach, B. J. Lee, Phase-field modeling for 3D grain growth based on a grain boundary energy database, Modelling and Simulation in Materials Science and Engineering 22 (3) (2014). doi:10.1088/0965-0393/22/3/034004.

[18] E. Miyoshi, T. Takaki, Extended higher-order multi-phase-field model for three-dimensional anisotropic-grain-growth simulations, Computational Materials Science 120 (2016) 77–83. doi:10.1016/j.commatsci.2016.04.014.
URL http://dx.doi.org/10.1016/j.commatsci.2016.04.014

[19] E. Miyoshi, T. Takaki, Multi-phase-field study of the effects of anisotropic grain-boundary properties on polycrystalline grain growth, Journal of Crystal Growth 474 (November 2016) (2017) 160–165. doi:10.1016/j.jcrysgro.2016.11.097.
URL http://dx.doi.org/10.1016/j.jcrysgro.2016.11.097

[20] K. Chang, L. Q. Chen, C. E. Krill, N. Moelans, Effect of strong nonuniformity in grain boundary energy on 3-D grain growth behavior: A phase-field simulation study, Computational Materials Science 127 (2017) 67–77. doi:10.1016/j.commatsci.2016.10.027.
URL http://dx.doi.org/10.1016/j.commatsci.2016.10.027

[21] K. Chang, H. Chang, Effect of grain boundary energy anisotropy in 2D and 3D grain growth process, Results in Physics 12 (January) (2019) 1262–1268. doi:10.1016/j.rinp.2019.01.028.
URL https://doi.org/10.1016/j.rinp.2019.01.028

[22] H. Salama, J. Kundin, O. Shchyglo, V. Mohles, K. Marquardt, I. Steinbach, Role of inclination dependence of grain boundary energy on the microstructure evolution during grain growth, Acta Materialia 188 (2020) 641–651. doi:10.1016/j.actamat.2020.02.043.

[23] A. L. Cruz-Fabiano, R. Logé, M. Bernacki, Assessment of simplified 2D grain growth models from numerical experiments based on a level set framework, Computational Materials Science 92 (2014) 305–312. doi:10.1016/j.commatsci.2014.05.060.
URL http://dx.doi.org/10.1016/j.commatsci.2014.05.060

[24] M. Elsey, S. Esedo, P. Smereka, Large Scale Simulations and Parameter Study for a Simple Recrystallization Model, Philosophical Magazine (2010) 1–31.

[25] M. Elsey, S. Esedoglu, P. Smereka, Simulations of anisotropic grain growth: Efficient algorithms and misorientation distributions, Acta Materialia 61 (6) (2013) 2033–2043. doi:10.1016/j.actamat.2012.12.023.
URL http://dx.doi.org/10.1016/j.actamat.2012.12.023

[26] H. Hallberg, Influence of anisotropic grain boundary properties on the evolution of grain boundary character distribution during grain growth - A 2D level set study, Modelling and Simulation in Materials Science and Engineering 22 (8) (2014). doi:10.1088/0965-0393/22/8/085005.

[27] S. Esedoglu, F. Otto, Threshold Dynamics for Arbitrary Surface Tensions, Comm Pure Appl Math 68 (5) (2015) 808–864. doi:10.1002/cpa.21527.

[28] J. Fausty, N. Bozzolo, D. Pino Muñoz, M. Bernacki, A novel level-set finite element formulation for grain growth with heterogeneous grain boundary energies, Materials and Design 160 (2018) 578–590. doi:10.1016/j.matdes.2018.09.050.
URL https://doi.org/10.1016/j.matdes.2018.09.050

[29] J. Fausty, N. Bozzolo, M. Bernacki, A 2D level set finite element grain coarsening study with heterogeneous grain boundary energies, Applied Mathematical Modelling 78 (2020) 505–518. doi:10.1016/j.apm.2019.10.008.
URL https://doi.org/10.1016/j.apm.2019.10.008

[30] X. Zhang, J. S. Chen, S. Osher, A multiple level set method for modeling grain boundary evolution of polycrystalline materials, Interaction and Multiscale Mechanics 1 (2) (2008) 191–209. doi:10.12989/imm.2008.1.2.191.
URL ftp://www.math.ucla.edu/pub/camreport/cam06-69.pdf%5Cnftp://ftp.math.ucla.edu/pub/camreport/cam06-69.pdf

[31] H. Hallberg, V. V. Bulatov, Modeling of grain growth under fully anisotropic grain boundary energy, Modelling and Simulation in Materials Science and Engineering (2019). doi:10.1088/1361-651X/ab0c6c.
URL https://doi.org/10.1088/1361-651X/ab0c6c

[32] C. Mießen, M. Liesenjohann, L. A. Barrales-Mora, L. S. Shvindlerman, G. Gottstein, An advanced level set approach to grain growth - Accounting for grain boundary anisotropy and finite triple junction mobility, Acta Materialia 99 (2015) 39–48. doi:10.1016/j.actamat.2015.07.040.

[33] F. Wakai, N. Enomoto, H. Ogawa, Three-dimensional microstructural evolution in ideal grain growth general statistics, Acta Materialia 48 (6) (2000) 1297–1311. doi:10.1016/S1359-6454(99)00405-X.

[34] E. A. Lazar, R. D. Macpherson, D. J. Srolovitz, A more accurate two-dimensional grain growth algorithm, Acta Materialia 58 (2) (2010) 364–372. doi:10.1016/j.actamat.2009.09.008.
URL http://dx.doi.org/10.1016/j.actamat.2009.09.008

[35] E. A. Lazar, J. K. Mason, R. D. Macpherson, D. J. Srolovitz, A more accurate three-dimensional grain growth algorithm, Acta Materialia 59 (17) (2011) 6837–6847. doi:10.1016/j.actamat.2011.07.052.
URL http://dx.doi.org/10.1016/j.actamat.2011.07.052

[36] A. Kuprat, D. George, G. Straub, M. C. Demirel, Modeling microstructure evolution in three dimensions with Grain3D and LaGriT, Computational Materials Science 28 (2) (2003) 199–208. doi:10.1016/S0927-0256(03)00107-1.

[37] W. W. Mullins, Two-dimensional motion of idealized grain boundaries, Journal of Applied Physics 27 (8) (1956) 900–904. doi:10.1063/1.1722511.

[38] J. von Neumann, Seminar Report (Cleveland, Ohio: American Society for Metals) (1952).

[39] R. D. MacPherson, D. J. Srolovitz, The von Neumann relation generalized to coarsening of three-dimensional microstructures, Nature 446 (7139) (2007) 1053–1055. arXiv:t8jd4qr3m, doi:10.1038/nature05745.

[40] C. E. K. Iii, L. Chen, Computer simulation of 3-D grain growth using a phase- field model, Acta Materiala 50 (2002) 3057–3073.

[41] Read-Shockley, Dislocation Models of crystal grain boundaries, Physical review (1950).

[42] H.-K. Kim, W.-S. Ko, H.-J. Lee, S. G. Kim, B.-J. Lee, An identification scheme of grain boundaries and construction of a grain boundary energy database, Scripta Materialia 64 (12) (2011) 1152–1155.

[43] G. Caginalp, The role of microscopic anisotropy in the macroscopic behavior of a phase boundary, Annals of Physics 172 (1) (1986) 136–155.

[44] V. V. Bulatov, B. W. Reed, M. Kumar, Grain boundary energy function for fcc metals, Acta Materialia 65 (February) (2014) 161–175. doi:10.1016/j.actamat.2013.10.057.
URL http://dx.doi.org/10.1016/j.actamat.2013.10.057

[45] S. G. Baird, E. R. Homer, D. T. Fullwood, O. K. Johnson, Five degree-of-freedom property interpolation of arbitrary grain boundaries via voronoi fundamental zone framework, Computational Materials Science 200 (2021) 110756. doi:https://doi.org/10.1016/j.commatsci.2021.110756.
URL https://www.sciencedirect.com/science/article/pii/S0927025621004833

[46] D. L. Olmsted, S. M. Foiles, E. A. Holm, Survey of computed grain boundary properties in face-centered cubic metals: I. grain boundary energy, Acta Materialia 57 (13) (2009) 3694–3703.

[47] V. Mohles, 3-D front tracking model for interfaces with anisotropic energy, Computational Materials Science 176 (2020) 109534. doi:10.1016/j.commatsci.2020.109534.

[48] J. Hirsch, T. Al-Samman, Superior light metals by texture engineering: Optimized aluminum and magnesium alloys for automotive applications, Acta Materialia 61 (3) (2013) 818–843.

[49] T. Al-Samman, G. Gottstein, Dynamic recrystallization during high temperature deformation of magnesium, Materials Science and Engineering: A 490 (1-2) (2008) 411–420.

[50] E. Ball, P. Prangnell, Tensile-compressive yield asymmetries in high strength wrought magnesium alloys, Scripta Metallurgica et Materialia;(United States) 31 (2) (1994).

[51] D. D. Sam, B. L. Adams, Orientation and strain dependence of stored energy of cold work in axisymmetric copper, Metallurgical Transactions A 17 (11) (1986) 1175–1179. doi:https://doi.org/10.1007/BF02643958.

[52] M. D. Sangid, A. Nicolas, K. Kapoor, E. Fodran, J. Madsen, Modeling the role of epitaxial grain structure of the prior $\beta$ phase and associated fiber texture on the strength characteristics of ti-6al-4v produced via additive manufacturing, Materials 13 (10) (2020) 2308.

[53] V. Radmilovic, U. Dahmen, D. Gao, C. R. Stoldt, C. Carraro, R. Maboudian, Formation of¡ 111¿ fiber texture in $\beta$-sic films deposited on si (100) substrates, Diamond and related materials 16 (1) (2007) 74–80.

[54] M. Cheng, X. Xiao, G. Luo, L. Song, Integrated control of molten pool morphology and solidification texture by adjusting pulse duration in laser additive manufacturing of inconel 718, Optics & Laser Technology 142 (2021) 107137.

[55] G. Nolze, R. Hielscher, Orientations – perfectly colored, Journal of Applied Crystallography 49 (5) (2016) 1786–1802. doi:10.1107/S1600576716012942.
URL https://doi.org/10.1107/S1600576716012942

[56] W. Bollmann, Triple lines in polycrystalline aggregates as disclinations, Philosophical Magazine A 49 (1) (1984) 73–79. arXiv:https://doi.org/10.1080/01418618408233430, doi:10.1080/01418618408233430.
URL https://doi.org/10.1080/01418618408233430

[57] J. K. Mason, C. A. Schuh, Correlated grain-boundary distributions in two-dimensional networks, Acta Crystallographica Section A 63 (4) (2007) 315–328. doi:10.1107/S0108767307021782.
URL https://doi.org/10.1107/S0108767307021782

[58] M. A. Groeber, M. A. Jackson, DREAM.3D: A Digital Representation Environment for the Analysis of Microstructure in 3D, Integrating Materials and Manufacturing Innovation 3 (1) (2014) 5. doi:10.1186/2193-9772-3-5.
URL http://link.springer.com/10.1186/2193-9772-3-5

[59] W. E. Lorensen, H. E. Cline, Marching cubes: A high resolution 3d surface construction algorithm, ACM siggraph computer graphics 21 (4) (1987) 163–169.

[60] S. Maddali, S. Ta'asan, R. M. Suter, Topology-faithful nonparametric estimation and tracking of bulk interface networks, Computational Materials Science 125 (2016) 328–340. arXiv:1601.04699, doi:10.1016/j.commatsci.2016.08.021.

[61] G. Taubin, Curve and surface smoothing without shrinkage, in: Proceedings of IEEE international conference on computer vision, IEEE, 1995, pp. 852–857.

[62] E. J. Lieberman, A. D. Rollett, R. A. Lebensohn, E. M. Kober, Calculation of grain boundary normals directly from 3D microstructure images, Modelling and Simulation in Materials Science and Engineering 23 (3) (2015). doi:10.1088/0965-0393/23/3/035005.

[63] T. Tasdizen, R. Whitaker, P. Burchard, S. Osher, Geometric surface processing via normal maps, ACM Trans. Graph. 22 (4) (2003) 1012–1033. doi:10.1145/944020.944024.
URL https://doi.org/10.1145/944020.944024

[64] C. Herring, Chapter 8 in the physics of powder metallurgy, MacGraw-Hill, New-York (1951) 143.

[65] K. Chang, N. Moelans, Effect of grain boundary energy anisotropy on highly textured grain

structures studied by phase-field simulations, Acta Materialia 64 (2014) 443–454. doi:10.1016/j.actamat.2013.10.058.

[66] J. Zhang, Y. Zhang, W. Ludwig, D. Rowenhorst, P. W. Voorhees, H. F. Poulsen, Three-dimensional grain growth in pure iron. Part I. statistics on the grain level, Acta Materialia 156 (2018) 76–85. doi:10.1016/j.actamat.2018.06.021.
URL https://doi.org/10.1016/j.actamat.2018.06.021

[67] Dingley, Randle, Microtexture determination by electron back-scatter diffraction, Journal of Materials Science 27 (1992).

[68] M. Frary, C. A. Schuh, Percolation and statistical properties of low- and high-angle interface networks in polycrystalline ensembles, Phys. Rev. B 69 (2004) 134115. doi:10.1103/PhysRevB.69.134115.
URL https://link.aps.org/doi/10.1103/PhysRevB.69.134115

[69] J. Mackenzie, Second paper on statistics associated with the random disorientation of cubes, Biometrika 45 (1-2) (1958) 229–240.

[70] M. E. Frary, C. A. Schuh, Correlation-space description of the percolation transition in composite microstructures, Physical Review E - Statistical, Nonlinear, and Soft Matter Physics 76 (4) (2007). doi:10.1103/PhysRevE.76.041108.

[71] M. Frary, C. A. Schuh, Grain boundary networks: Scaling laws, preferred cluster structure, and their implications for grain boundary engineering, Acta Materialia 53 (16) (2005) 4323–4335. doi:https://doi.org/10.1016/j.actamat.2005.05.030.
URL https://www.sciencedirect.com/science/article/pii/S1359645405003319

[72] J. K. Mason, C. A. Schuh, Correlated grain-boundary distributions in two-dimensional networks, Acta Crystallographica Section A 63 (4) (2007) 315–328. doi:10.1107/S0108767307021782.
URL https://doi.org/10.1107/S0108767307021782

[73] V. Randle, G. S. Rohrer, H. M. Miller, M. Coleman, G. T. Owen, Five-parameter grain boundary distribution of commercially grain boundary engineered nickel and copper, Acta Materialia 56 (10) (2008) 2363–2373. doi:10.1016/j.actamat.2008.01.039.

[74] N. Bernstein, The influence of geometry on grain boundary motion and rotation, Acta Materialia 56 (5) (2008) 1106–1113. doi:https://doi.org/10.1016/j.actamat.2007.11.002.
URL https://www.sciencedirect.com/science/article/pii/S1359645407007628

[75] H. Sharma, R. M. Huizenga, A. Bytchkov, J. Sietsma, S. E. Offerman, Observation of changing crystal orientations during grain coarsening, Acta Materialia 60 (1) (2012) 229–237. doi:https://doi.org/10.1016/j.actamat.2011.09.057.
URL https://www.sciencedirect.com/science/article/pii/S135964541100704X

[76] M. Upmanyu, D. Srolovitz, A. Lobkovsky, J. Warren, W. Carter, Simultaneous grain boundary migration and grain rotation, Acta Materialia 54 (7) (2006) 1707–1719. doi:https://doi.org/10.1016/j.actamat.2005.11.036.
URL https://www.sciencedirect.com/science/article/pii/S135964540500707X